THE NUCLEAR SPIN DEPENDENCE OF THE REACTION OF H_3^+ WITH H_2 AND THE PROPOSED SPECTROSCOPIC INVESTIGATION OF HO_2^+

BY

CARRIE A. KAUFFMAN

THESIS

Submitted in partial fulfillment of the requirements
for the degree of Master of Science in Chemistry
in the Graduate College of the
University of Illinois at Urbana-Champaign, 2011

Urbana, Illinois

Adviser:

Assistant Professor Benjamin J. McCall

Abstract

High-resolution spectroscopy of molecular ions has been proven to be a difficult endeavor. Generating significant quantities of the desired ions and discriminating ions from neutrals are among some of the many difficulties surrounding the spectroscopic studies of these species. Despite these difficulties, molecular ions and their reactions play important roles as intermediates in organic reactions, reactants in combustion chemistry, species in biological processes such as respiration, as interstellar species, and as species found in terrestrial and extraterrestrial atmospheres. Although extensive research has been devoted to study these species and their reactions, scientists have barely "scratched the surface" in the realm of molecular ions.

One of the simplest molecular ions, H_3^+, has been measured spectroscopically in the laboratory and observed by astronomers in the interstellar medium, the galactic center, and planetary atmospheres. Both H_3^+ and its parent neutral, H_2, exist in two nuclear spin configurations, *ortho* and *para*, and yield unique spectral signatures that can be measured in the laboratory and in astronomical environments. Most importantly, these species have been found to be useful temperature probes of interstellar clouds. However, a temperature discrepancy arises when comparing the temperatures calculated from each species. Since the chemistry of H_2 has been well established, these findings indicate that the regulation of the nuclear spin states of H_3^+ is not well understood.

The nuclear spin configuration of interstellar H_3^+ is postulated to be governed by the reaction of $H_3^+ + H_2 \rightarrow H_2 + H_3^+$ and is one of the topics explored in this work. This reaction is investigated in the laboratory by spectroscopically monitoring the populations of several low-energy levels of *ortho*- and *para*-H_3^+ in hydrogenic plasmas of varying *para*-H_2 enrichments. Measurements were taken at room temperature and for the first time, at liquid nitrogen temperatures. Steady-state modeling is employed to infer the ratio of the rates of the hop and exchange pathways of the above reaction and aids in the understanding of how the distribution of the nuclear spin states of H_3^+ is regulated in the interstellar medium. This study will aid in understanding of the temperature discrepancy found between H_2 and H_3^+ in hopes to improve the viability of H_3^+ as a temperature probe in astronomical environments where H_2 measurements are impossible or not readily available.

Finally, a larger polyatomic molecular ion, HO_2^+, will be discussed in the final chapter. Although many simple polyatomic ions have been studied, the species HO_2^+ has eluded detection for nearly three decades. Given the current theoretical information and past experimental attempts, a proposed experiment for the detection of this species is outlined.

To my beloved Grandmother, Harriet J. Piontkowski.

Acknowledgments

I would like to first and forth most like to thank my advisor, Dr. Benjamin McCall, for his encouragement, support, and guidance throughout my graduate career. He has truly helped shape the scientist I am today.

I am also immensely thankful for all the McCall Group Members for their knowledge, support, and humorous conversations. In particular, I would like to thank Kyle Crabtree for his patience and mentorship throughout the various projects we shared. To Mike Harland and the rest of the School of Chemical Sciences Machine Shop for their guidance on the various designs submitted for this work.

Finally, I would like thank my family for their constant support. To my mother and father who supported me throughout all my trials and tribulations and for their unconditional love that helped me get through the toughest times. I am also blessed to have a sister that would "lend an ear" even if she didn't understand the science. I also would like to thank my grandmother, who without her, I would not have had the financial means and confidence to have accomplished what I have thus far. I would like to thank my husband, Tony, for standing by me throughout all my schooling and pushing me all the way to the end. And finally, I would like to thank my daughter, Arielle, for being a constant motivation to succeed.

Contents

List of Tables

List of Figures

Chapter 1

Introduction to the $H_3^+ + H_2$ Reaction

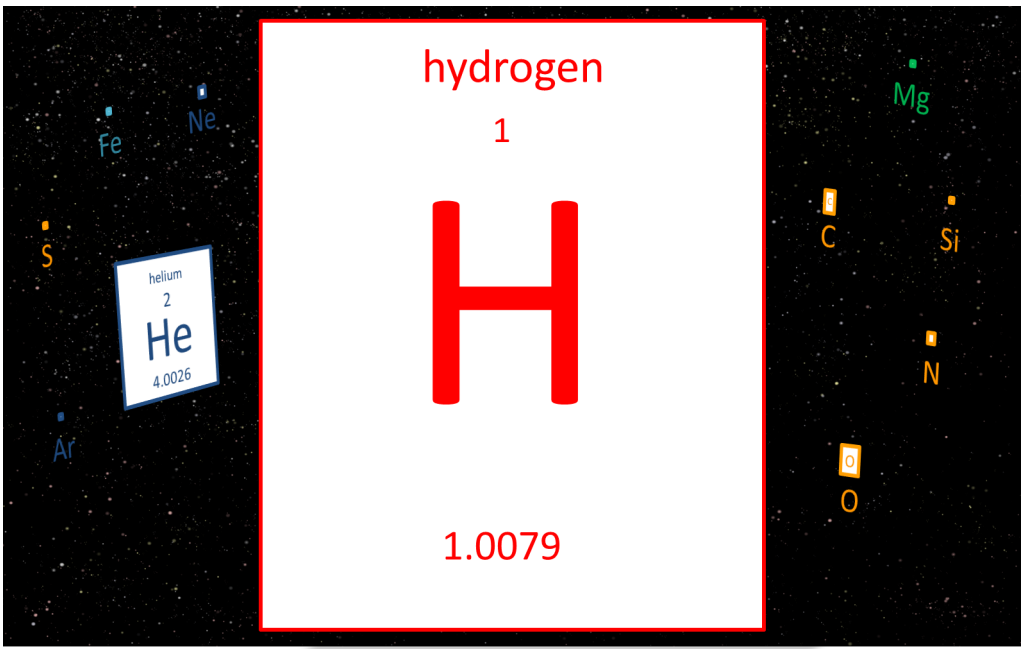

Figure 1.1: An adapted version of the periodic table to reflect the cosmic abundances [35].

Constituting 90 % of the Universe's atoms, hydrogen is by far the most abundant element. If one were to modify the periodic table to incorporate the cosmic abundance of each element, it would closely resemble Figure 1.1 [60, 35]. As the dominant element in the Universe, hydrogen and its derivatives play an important role in astrochemistry. Initially, it was thought that interstellar hydrogen mostly existed in atomic form, but it was later determined to exist primarily in molecular form [41]. When molecular hydrogen is subjected to omnipresent cosmic rays in interstellar clouds, it undergoes ionization yielding the short-lived H_2^+ ion. This short lifetime is due to the fact that it quickly and efficiently reacts with a neighboring H_2 molecule to generate one of the dominant hydrogenic species, H_3^+. First astronomically observed in 1996, this species has a very low proton affinity of 4.4 eV and as a result, it is regarded as an universal proton donor. This has led to many scientists postulating that H_3^+ initiates a sequence of ion-neutral reactions that results in

the formation of larger polyatomics in the interstellar medium [41, 26, 63].

Not only has the study of hydrogenic species proven to be valuable in understanding the chemistry that is occurring in our universe, but the study of hydrogenic species has proven to be a valuable tool in astronomy for determining interstellar cloud dimensions, estimating cloud densities, and inferring the cosmic ray ionization rate. Additionally, the two nuclear spin configurations of both species, H_2 and H_3^+, can be used to derive temperatures of interstellar clouds [30, 54, 48, 49]. When comparing the two derived temperatures for diffuse clouds, a puzzling $30-40$ Kelvin temperature gap is discovered. Since it is already firmly established that H_2 is thermalized efficiently by the reaction of H_2 with H^+ in diffuse clouds [12], our understanding in the regulation of the nuclear spin states of H_3^+ is called into question. In fact, a recent steady-state modeling of the hydrogen chemistry has postulated that this discrepancy is due to the incomplete equilibration of the H_3^+ ion by reaction 1.1 [9]. In order to fully understand the chemistry that is occurring and to establish H_3^+ as a useful temperature probe, the nuclear spin dependence of the steady-state reaction 1.1 is experimentally investigated in cold laboratory plasmas, and is the subject of this work. In the following sections, both reactants will be discussed as well as the current knowledge of the reaction of H_3^+ with H_2 (1.1).

$$H_3^+ + H_2 \rightarrow H_2 + H_3^+ \tag{1.1}$$

1.1 H_2

The hydrogen molecule has a very simple molecular structure consisting of 2 protons and 2 electrons. Due to its simplicity, it has been a cornerstone in many chemical theories and studies. For instance, molecular hydrogen was one of the first quantum effects observed by Maxwell in his specific heat capacity study [58, 3]. Even today, hydrogen is a common benchmark species for testing computational techniques in quantum mechanics and many areas of chemistry and physics are still devoted to the research of molecular hydrogen.

The hydrogen molecule exists in two configurations based on their nuclear spin modifications. Since each proton has a nuclear spin of $I = 1/2$, the total nuclear spin of the hydrogen molecule can be calculated by vector addition. When their spins are anti-symmetrically aligned ($I = \frac{1}{2} - \frac{1}{2} = 0$), the species is referred to as *para*-hydrogen. Conversely, when their spins are symmetrically aligned ($I = \frac{1}{2} + \frac{1}{2} = 1$), the species is referred to as *ortho*-hydrogen. Since the interchange between spin states does not readily occur except by chemical reaction [50, 23] or in the presence of an inhomogeneous magnetic field [67], each nuclear spin state can be treated as separate chemical species. At room temperature, "normal"-hydrogen exist in a 3:1

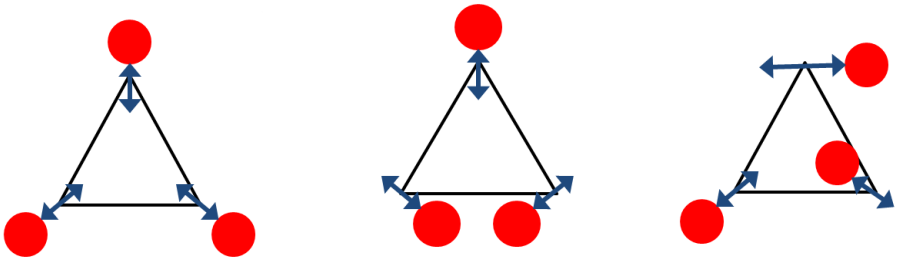

(a) The symmetric stretch or ν_1 mode of H_3^+

(b) Doubly-degenerate asymmetric stretch or ν_2 mode of H_3^+

Figure 1.2: Normal modes of H_3^+

ortho:*para* ratio.

Due to the lack of a dipole moment, no pure rotational and no "dipole-allowed" transitions can be observed for this species. Electronic transitions have been studied in the ultraviolet as well as the weak quadrupole vibrational transition in the mid-infrared [56, 55, 32, 6], but none of these methods are employed in this study. Instead, H_3^+ is used to investigate reaction 1.1 and will be discussed in the following section.

1.2 H_3^+

H_3^+ is the simplest polyatomic ion that consists of 3 protons and 2 electrons. It was first observed in a laboratory plasma in 1911 by J. J. Thomson using early mass spectrometric techniques. Shortly thereafter, it was determined that the reaction between H_2 and the cation H_2^+ results in the formation of H_3^+ and this reaction was determined to be exothermic with a very fast rate coefficient [59, 28]. Correspondingly, H_3^+ was first detected in molecular clouds in 1996 followed shortly by numerous other detections in both diffuse and dense molecular clouds [20, 36, 22]. Additionally, it has been thought to play an important role in the ionospheres of Jupiter, Uranus, and Saturn [15, 62, 21]. With these planets, H_3^+ has also been postulated to play an important role in the cooling process of the upper atmospheres [38]. Thus, it can be concluded that H_3^+ is found in a diverse set of astronomical environments, but also has been studied in low pressure hydrogenic laboratory plasmas as well [41].

Like the parent molecule H_2, the H_3^+ ion exists in two nuclear spin configurations resulting from the various arrangements of the three nuclear spins of the hydrogen atoms. When two of the spins are aligned anti-symmetrically ($I = \frac{1}{2}$), it is referred to as *para*-H_3^+. When all spins are aligned symmetrically ($I = \frac{3}{2}$), the species is referred to as *ortho*-H_3^+. Similar to H_2, each nuclear spin state is treated as a separate chemical species.

Table 1.1: Selection Rules of H_3^+

Selection Rules
$\Delta k = 2n \pm 1$
$\Delta I = 0$, $\Delta g = 3n$
$\Delta J = 0, \pm 1$
$J = 0 \nleftrightarrow J = 0$

As a general rule, a non-linear polyatomic molecule has $3N - 6$ normal modes. Given $N = 3$ for H_3^+, it will have 3 normal modes (See Figure 1.2). The first mode, designated as v_1, is the breathing mode. In this mode, all hydrogen bonds expand and contract in unison. Due to the symmetry of this mode (A_1), it is infrared inactive and thus not useful for this investigation. The next mode, v_2 (E), corresponds to the anti-symmetric stretch and is a doubly degenerate infrared active mode. This mode also has vibrational angular momentum of $\pm l$, which couples with the rotational manifold resulting in the splitting of the rotational levels in the vibrational states of $v_2 > 0$. Overall, this provides a very useful rovibrational spectrum that can be used to probe this species and reaction 1.1. Unlike its parent species, H_2, it can be shown that the ion H_3^+ has a spin degeneracy ratio of 2:1. Due to having E symmetry, the states of p-H_3^+ are doubly degenerate and this adds an additional factor of 2 to the total degeneracy. This effectively cancels the spin degeneracy ratio and results in a 1:1 *ortho*:*para* ratio of H_3^+ in a normal H_2 plasma.

To understand the notation used to describe the various levels studied in this investigation, it is necessary to briefly summarize the selection rules of H_3^+ for dipole-allowed transitions. Selection rules can be derived by the use of the electric dipole operator, $\hat{\mu}$, and are listed in Table 1.1. The quantum number g is defined to be the quantity $k - l$ where k is the projection of the rotational quantum number J onto the molecular axis. Due to the selection rules $\Delta k = 2n \pm 1$ and $\Delta g = 3n$ (where the quantity n can be unique to each expression), a change in angular momentum $\Delta l = \pm 1$ and $\Delta k = \pm 1$ implies that $\Delta g = 0$. Since the fundamental band is exclusively studied in this work, these are the only selection rules necessary to consider. When studying the excited vibrational levels where $\Delta l > 1$, an increase in the Coriolis coupling with the higher l mixes to a degree at which k is no longer a 'good' quantum number and the quantum number g is used instead. However, g is not always uniquely defined for each level under the condition $J - 1 \geq |g| \geq 1$ and results in two sets of quantum numbers of k and l that have the same g. To distinguish these levels, they can be labeled u and l for the upper and lower states respectively. Hence, the rovibrational transitions are labeled in this work in the following notation:

$$R(J, G)^{u|l}$$

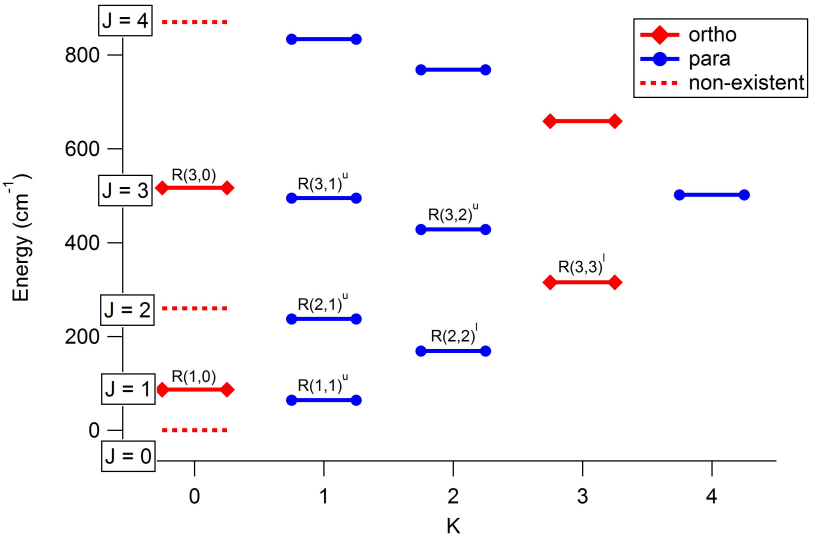

Figure 1.3: A diagram of the ground state energy levels of H_3^+

where R represents the transition in which $\Delta J = +1$, J is the rotational quantum number, $G = |g|$ and equal is to $|k|$ when in the the ground vibrational state, and the $u|l$ defines the upper and lower states as stated previously. A more in-depth derivation on the notation and group theory of both H_2 and H_3^+ can be found elsewhere [34, 60, 35]. The transitions studied in this investigation are listed in Table 2.1 and a diagram of the ground state energy levels of these transitions can be seen in Figure 1.3.

1.3 $H_3^+ + H_2 \rightarrow H_2 + H_3^+$

Reaction 1.1 was previously postulated as the reaction that regulates the nuclear spin states of the H_3^+ ion observed in the interstellar medium. Numerous works have been published on this reaction including papers on the group theory and statistical treatment of the reaction [45, 40, 42], 400 K measurements [8], and colder measurements using deuterium [24, 25, 29]. Additionally, studies have stated that the *ortho*:*para* ratio observed in the interstellar medium may influence deuterium fractionation in dense clouds [25]. This is due to the fact that the deuteration of H_3^+ has been shown to be strongly influenced by the amount of *ortho*-H_2. Thus, not only does the study of this reaction provide insight into the apparent *para*-enrichment observed in the interstellar medium and as a potential temperature probe, but also an insight into the deuteration of many interstellar species. Therefore, additional experimental measurements of this reaction at colder and more relevant temperatures is important.

Before the experimental investigation can be discussed, it important to theoretically determine the spin-branching ratio of reaction 1.1. As discussed in last two sections, the degeneracies of H_2 and H_3^+ spin

modifications can be calculated based on their symmetry. Extending this idea, it is also possible to calculate the statistical outcome of this reaction given the initial spin modifications of the reactants. Although group theory can be used to calculate these statistical weights [45], a simpler method is discussed here. This method was published in 2004 by T. Oka and employs the use of angular momentum algebra [40]. A brief summary of this method will be discussed followed by a summary of the results.

To calculate the statistical weights using Oka's method, the following formula, also known as the almighty formula, is used.

$$\mathcal{D}_{I_1} \otimes \mathcal{D}_{I_2} = \mathcal{D}_{I_1+I_2} \oplus \mathcal{D}_{I_1+I_2-1} \oplus \cdots \oplus \mathcal{D}_{|I_1-I_2|}, \tag{1.2}$$

The $\mathcal{D}_I$ represents the nuclear spin modification. This formula is applied to each reactant in reaction 1.1. For example, the reactant H_3^+ results in the following:

$$\mathcal{D}_{1/2} \otimes \mathcal{D}_{1/2} \rightarrow \mathcal{D}_1 \oplus \mathcal{D}_0$$
$$(\mathcal{D}_1 \oplus \mathcal{D}_0) \otimes \mathcal{D}_{1/2} \rightarrow \mathcal{D}_{3/2} \oplus 2\mathcal{D}_{1/2}$$

A similar procedure can be applied to the other reactant, H_2, and combination of these two expression results in the overall expression for the reactants of reaction 1.1:

$$(\mathcal{D}_{3/2} \oplus 2\mathcal{D}_{1/2}) \otimes (\mathcal{D}_1 \oplus \mathcal{D}_0) \rightarrow \mathcal{D}_{5/2} \oplus 4\mathcal{D}_{3/2} \oplus 5\mathcal{D}_{1/2}. \tag{1.3}$$

Note, $(\mathcal{D}_{3/2} \oplus 2\mathcal{D}_{1/2})$ is written to represent the H_3^+ reactant and $(\mathcal{D}_1 \oplus \mathcal{D}_0)$ represents the H_2 reactant. The factor of 2 on the $\mathcal{D}_{1/2}$ term is needed to account for the fact that there is twice the amount of *para*-H_3^+ states as there are for *ortho*-H_3^+. The same expression can be derived for the product side of this reaction due to having the same products as reactants. The next step in this method is to reduce the expression into its constituent parts as shown below:

$$\mathcal{D}_{3/2} \otimes \mathcal{D}_1 \rightarrow \mathcal{D}_{5/2} \oplus \mathcal{D}_{3/2} \oplus \mathcal{D}_{1/2}$$
$$\mathcal{D}_{3/2} \otimes \mathcal{D}_0 \rightarrow \mathcal{D}_{3/2}$$
$$2\mathcal{D}_{1/2} \otimes \mathcal{D}_1 \rightarrow 2\mathcal{D}_{3/2} \oplus 2\mathcal{D}_{1/2}$$
$$2\mathcal{D}_{1/2} \otimes \mathcal{D}_0 \rightarrow 2\mathcal{D}_{1/2}.$$

It is then necessary to balance the degeneracies and coefficients of the terms belonging to the H_5^+ intermediate

and results in the following expressions:

$$\mathcal{D}_{5/2} \rightarrow 6(\mathcal{D}_{3/2} \otimes \mathcal{D}_1/12)$$

$$\mathcal{D}_{3/2} \rightarrow (\mathcal{D}_{3/2} \otimes \mathcal{D}_1/12) \oplus (\mathcal{D}_{3/2} \otimes \mathcal{D}_0/4) \oplus 2(\mathcal{D}_{1/2} \otimes \mathcal{D}_1/6)$$

$$\mathcal{D}_{1/2} \rightarrow 2/5(\mathcal{D}_{3/2} \otimes \mathcal{D}_1/12) \oplus 4/5(\mathcal{D}_{1/2} \otimes \mathcal{D}_1/6) \oplus 4/5(\mathcal{D}_{1/2} \otimes \mathcal{D}_0/2).$$

With both sets of expressions derived, it is then possible to determine the statistical weights for the various combinations of *ortho* and *para*-H_3^+ reacting with *ortho* and *para*-H_2 by simply substituting the resulting products with the expressions for the H_5^+ intermediate products. From this, the statistical weights of the reactions can be calculated. The results of all possible reactions are shown in Table 1.2.

Reactants	Weight	o-$H_3^+ + o$-H_2	$o + p$	$p + o$	$p + p$
o-$H_3^+ + o$-H_2	12	37/5	1	14/5	4/5
o-$H_3^+ + p$-H_2	4	1	1	2	0
$2(p$-$H_3^+ + o$-$H_2)$	12	14/5	2	28/5	8/5
$2(p$-$H_3^+ + p$-$H_2)$	4	4/5	0	8/5	8/5

Table 1.2: The product spin weights for $H_3^+ + H_2 \rightarrow H_3^+ + H_2$.

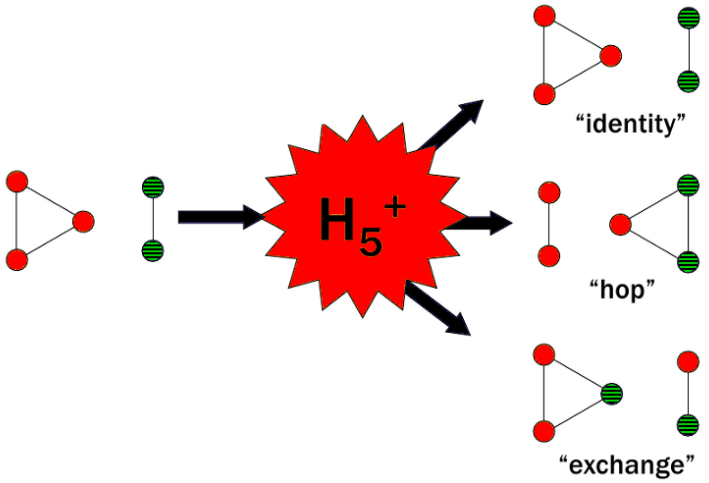

Figure 1.4: A schematic of various pathways (identity, hop, and exchange) of the reaction 1.1.

There is another important complication with reaction 1.1 that arises from the fact that there are three different pathways: the identity, the hop, and the exchange. These three pathways are demonstrated in Figure 1.4. Since there are 5 different protons in this reaction and two groups (one group of 2 and one group of 3), there are then $5!/3!2! = 10$ possible outcomes. By observing all of the possible combinations of protons in the products, this equates to 1 identity, 3 hops, and 6 exchanges. Using the previous derived statistical

Reactants	Weight		o-$H_3^+ + o$-H_2	o-$H_3^+ + p$-H_2	p-$H_3^+ + o$-H_2	p-$H_3^+ + p$-H_2
o-$H_3^+ + o$-H_2	12	ID	6/5	0	0	0
		Hop	12/5	0	6/5	0
		Exch	19/5	1	8/5	4/5
o-$H_3^+ + p$-H_2	4	ID	0	2/5	0	0
		Hop	0	0	6/5	0
		Exch	1	3/5	4/5	0
$2(p$-$H_3^+ + o$-$H_2)$	12	ID	0	0	6/5	0
		Hop	6/5	6/5	3/5	3/5
		Exch	8/5	4/5	19/5	1
$2(p$-$H_3^+ + p$-$H_2)$	4	ID	0	0	0	2/5
		Hop	0	0	3/5	3/5
		Exch	4/5	0	1	3/5

Table 1.3: Path-specific spin statistical weights for reaction 1.1.

weights, it is possible to derive path-specific spin statistical weights as can be seen in Table 1.3.

An additional table, Table 1.4, allows further insight into each of these pathways. For a given set of reactants, the product fractions of *ortho*- and *para*-H_3^+ is shown for each pathway. By inspection, a few key points become apparent. In the case of the identity pathways, no spin conversion takes place. This can be seen in Table 1.4 where each of the product spin fractions represented in the identity pathway results in a value of 1 corresponding to the same spin state of the H_3^+ reactant. For the exchange pathway, it is important to note that p-H_3^+ can be converted to o-H_3^+ and vice versa regardless of the spin states of the reactants (i.e. all non-zero product fractions for the exchange pathways in Table 1.4). This is not the same for the hop pathway. For a pure *para*-hydrogen plasma, it becomes evident that the exchange pathway becomes the dominant pathway for the production of *ortho*-H_3^+. It follows that the *para*-H_3^+ enrichment is strongly dependent on the relative rates of the hop and exchange pathways. Therefore, the value $\alpha = k_{hop}/k_{exchange}$ is defined and is the key quantity that is inferred in this investigation in order to understand the nuclear spin dependence of the reaction 1.1.

The following two chapters will outline the investigation of the nuclear spin dependence of reaction 1.1. Chapter 2 will introduce the various laboratory equipment used in this investigation as well as discuss the spectroscopic techniques that were used. Chapter 3 will conclude with the results of the experimental measurements and explain the steady-state modeling employed to infer the value of α. Finally, the implications of these measurements and future directions will be discussed.

Reactant Spin Modification and Pathway	Product Fractions *ortho*-H_3^+	*para*-H_3^+
ortho-H_3^++*ortho*-H_2		
Identity	1	0
Hop	2/3	1/3
Exchange	2/3	1/3
ortho-H_3^++*para*-H_2		
Identity	1	0
Hop	0	1
Exchange	2/3	1/3
para-H_3^++*ortho*-H_2		
Identity	0	1
Hop	2/3	1/3
Exchange	1/3	2/3
para-H_3^++*para*-H_2		
Identity	0	1
Hop	0	1
Exchange	1/3	2/3

Table 1.4: The product spin fractions for reaction 1.1.

Chapter 2

Experimental Details

In order to probe the nuclear spin dependence of the $H_3^+ + H_2 \rightarrow H_2 + H_3^+$ reaction, multipass direct absorption spectroscopy was performed on hydrogenic plasmas of varying *ortho*:*para* H_2 ratios. The transitions from the lowest energy rotational levels of H_3^+ of the v_2 fundamental band were measured (see Table 2.1), and the plasma kinetic temperature, the rotational temperature, and the fraction of p-H_3^+ (p_3) were calculated. The equipment that was necessary to perform these measurements were a *para*-hydrogen converter, a hollow cathode, and a difference frequency generation (DFG) laser (Figure 2.1). Each component will be discussed in the sections to follow in addition to the full details of the spectroscopy performed.

2.1 Para-Hydrogen Converter

Normal hydrogen gas (n-H_2, 25% p-H_2) was produced with a purity of 99.99999% by a hydrogen generator (Parker Balsten H2-1200). To produce $>$ 99.9% p-H_2 gas, a *para*-hydrogen converter, which is a modified closed-cycle ^{4}He cryostat constructed by a previous graduate student, Brian Tom, was used [61]. The cyrostat consists of oxygen-free high conductivity (OFHC) copper tubing that was filled with Fe_2O_3 catalyst. The tubing is wrapped around the cold head of the cryostat and held at 15 K. Normal hydrogen gas from the

Table 2.1: The rotational levels of H_3^+ and their target transitions in the v_2 fundamental band studied in this work [34]. Energies are relative to the forbidden (J,K) = (0,0) state.

Rotational State (J, K)	Type	Energy (cm^{-1})	Transition	Frequency (cm^{-1})
(1,1)	*para*	64.121	$R(1,1)^u$	2726.219
(1,0)	*ortho*	86.960	$R(1,0)$	2725.898
(2,2)	*para*	169.295	$R(2,2)^l$	2762.070
(2,1)	*para*	237.356	$R(2,1)^u$	2826.117
(3,3)	*ortho*	315.342	$R(3,3)^l$	2829.922
(3,2)	*para*	428.009	$R(3,2)^u$	2923.344
(3,1)	*para*	494.753	$R(3,1)^u$	2928.317
(3,0)	*ortho*	516.867	$R(3,0)$	2930.145

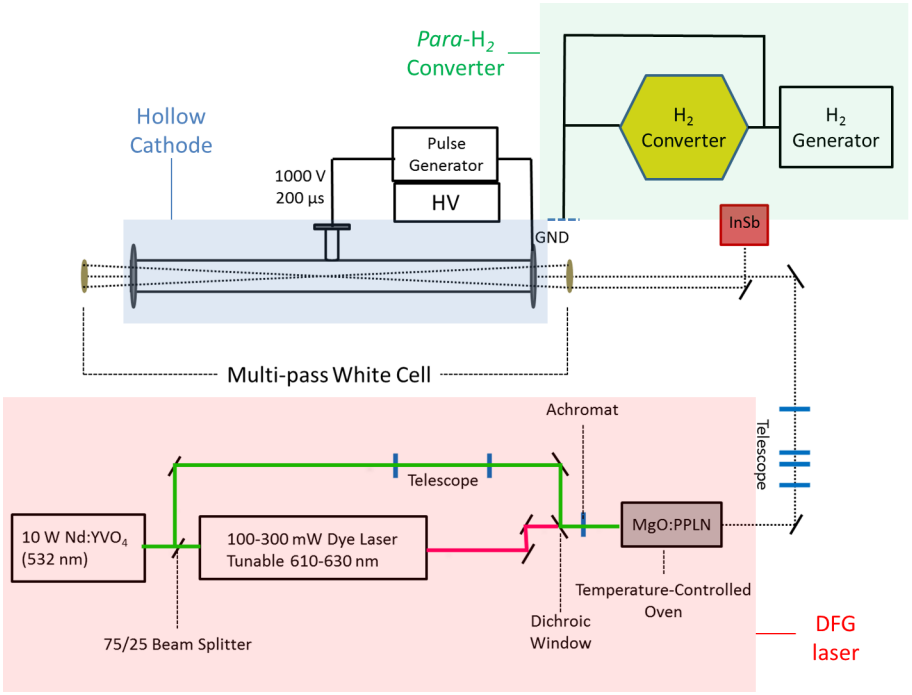

Figure 2.1: A diagram of the experimental set-up that includes the DFG, hollow cathode discharge cell, and the *para*-H_2 converter.

generator is passed through the copper tubing and over the catalyst to produce $> 99.9\%$ p-H_2 gas. Full details about this p-H_2 converter can be found elsewhere [61].

The n-H_2 and p-H_2 gas produced by the generator and converter respectively, were continuously fed to the hollow cathode for spectroscopic investigation. Mixtures of 40%, 50%, 66%, and 83% p-H_2 gas with uncertainies of $\pm 1.0\%$, 1.1%, 1.2%, and 1.4% respectively were produced by combining the appropriate partial pressures of p-H_2 and n-H_2 gas in a 1 liter gallon cylinder. To minimize the back-conversion of p-H_2 to o-H_2, the cylinder was lined with Teflon.

2.2 Hollow Cathode

The hollow cathode discharge was initially studied by Paschen in 1916 and has been subsequently studied as a spectroscopic ion source [43]. It has been found that the hollow cathode discharge has many advantages when compared to other ion sources such as an increased current density and discharge efficiency, a current that is weakly influenced by the gas pressure, and a lower operating voltage that results in lower temperature plasmas [14, 7]. As such, the hollow cathode discharge cell has been used extensively in spectroscopic studies of molecular ions [1, 19, 2].

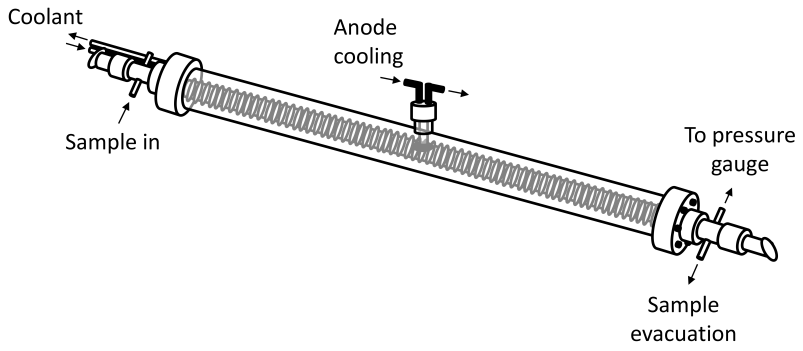

Figure 2.2: A schematic of hollow cathode cell used in this experiment.

The hollow cathode cell that was used in this experiment was constructed based on designs provided by Takayoshi Amano and built by an undergraduate student, Brett McGuire [37]. It has been used to produce pulsed hydrogenic plasmas and a schematic drawing of the cell can be seen in Figure 2.2.

2.2.1 Design

The cathode consists of a 1.4 m long, 1.5 in. diameter cylindrical copper tube tightly wrapped with 1/4 in. diameter copper tubing that allows for circulation of cooling/heating fluid to cool/heat the cathode. There is a 1 in. diameter hole located at the midpoint of the cathode to align with the anode. The cathode itself is encased in a 4 in. diameter, 1.6 m long, thick-walled glass tube and held in place by four Teflon spacers. The glass tube is terminated on each end by 4.625 in. conflat flanges that are custom machined to accept a smaller diameter glass tube. Of these two flanges, one is also welded with 1/4 in. Swagelok feedthroughs to attach the cathode cooling/heating lines.

The smaller diameter tubes located on the ends also have two glass appendages that allow for Ultra-Torr connections for sample input, sample evacuation, and a pressure gauge attachment. The ends of the glass tubes are connected by Ultra-Torr fittings to a hollow stainless steel tube cut at Brewster's angle (55.4°) at the outer end. Two BaF_2 windows are epoxied to these ends to allow laser light to pass through the cell.

The anode is water-cooled and attached to a 1 in. diameter appendage located at the midpoint of the cathode. By the use of a vespel ring and a smaller diameter quartz tube (hereafter called the guide tube), the anode is "guided" to the cathode to minimize arcing. A pulsed electrical discharge is generated by applying a 200 μs, 1 kV pulse to the anode at $\approx$ 1 Hz while grounding the cathode. The current was 1.25 A throughout the pulse with only subtle differences observed under the various cell pressure and temperature conditions (Figure 2.3).

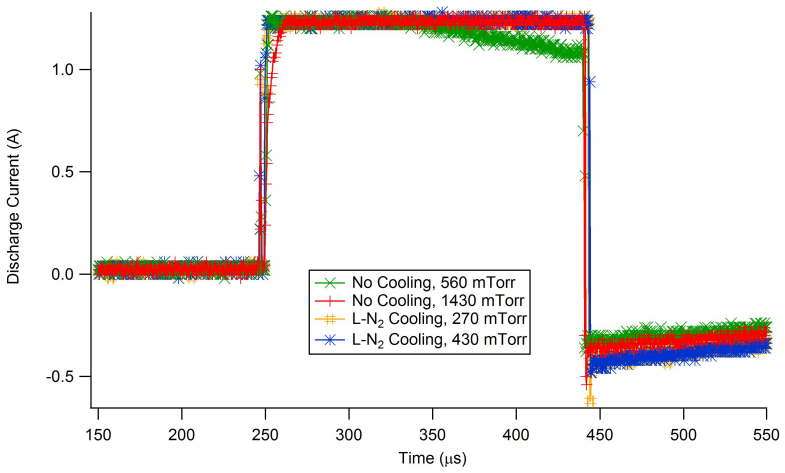

Figure 2.3: The current during the discharge pulse for the four main conditions used in this study. The negative spike after the pulse is due to electrical pick-up of the pulser box recharging.

2.2.2 Modifications

The insertion of the guide tube was successful in preventing arcing in earlier experiments performed by previous students, Brett McGuire and Brian Tom, but the success of the previous design was sensitive to the exact length of the guide tube. Due to fractures in the guide tube used in their experiments, more guide tubes were acquired for this experiment. To prevent arcing with the new guide tubes and thus improve the robustness of this component, the guide tubes were modified by tapering the end that is inserted into the cathode. A Teflon spacer was also partially inserted in the cathode orifice to minimize the exposure to any sharp edges. In addition to preventing arcing, this modification allowed more flexibility in the length of guide tube. A schematic drawing of this modification can be seen in Figure 2.4.

The welded joints that connected the coolant feedthroughs on the end flange also required modification. Upon cooling the cell using liquid nitrogen, large leaks would be induced into the system. In the original design, a butt weld, in which two flat edges are joined together end-on, was implemented (Figure 2.5) [5]. Though sufficient for most applications, the small depth of weld penetration results in thermal stress cracking points when subjected to liquid nitrogen temperatures. It was necessary to increase the strength of the weld by using a full penetration weld accomplished by beveling the adjoining edges on both faces and this is referred to as a double bevel weld (Figure 2.5). With this modification, the hollow cathode cell was capable of being cooled using liquid nitrogen for an indefinite period of time.

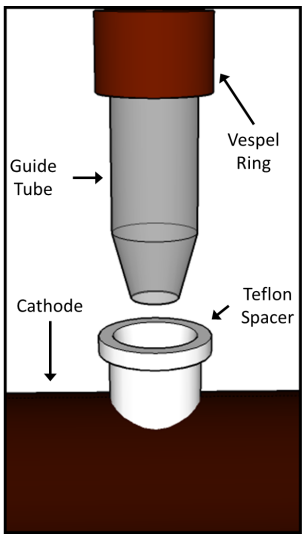

Figure 2.4: A three-dimensional rendering of the modified guide tube and Teflon insert.

(a) Schematic drawing of a butt weld.

(b) Schematic drawing of a double bevel weld.

Figure 2.5: Types of Welds

2.3 Difference Frequency Generation Laser

In order to generate tunable mid-infrared light, a process known as difference frequency generation was utilized [17]. In this process, two input optical beams at different frequencies are combined in a nonlinear crystal. Through nonlinear mixing, the difference frequency of the two input beams is generated. The DFG laser that was constructed in our lab is comprised of a frequency-doubled Nd:YVO_4 laser (Coherent Verdi V10), a tunable ring dye laser (Coherent 899-29), and a MgO-doped periodically poled $LiNbO_3$ crystal. By using various dyes in the ring dye laser, the DFG can generate tunable mid-infrared light in the range of 2.2 to 4.8 μm. For this study, the dye Rhodamine 640 (623 nm), was used and resulted in 500 μW of tunable 3.67 μm light.

2.4 Direct Absorption Spectroscopy and Analysis

Direct absorption spectroscopy is typically used to study time-dependent behavior of chemical systems [47, 18]. In low density samples where only a small fraction of the light is absorbed, this method becomes challenging. A simple solution is to increase the pathlength by the use of a multipass configuration. In this experiment, a White-type multipass configuration was employed. By the use of three mirrors, one that is placed one radius of curvature away from the other two, the beam traverses the cell in multiples of four and thereby increasing the pathlength. In addition to the increase in pathlength, the beam is also re-focused upon each traversal of the cell. This results in minimizing the losses to only scattering and absorption [65].

To use this technique, the mid-infrared light generated by DFG probed the plasma formed in the hollow cathode in the White-type multipass configuration. The resultant signal was detected by a cryogenically cooled dc InSb detector and then sent to a computer for analysis. The InSb signal was ratioed with the signal from a silicon photodiode that monitored the dye laser to remove pump laser amplitude noise. The full optical layout for this system can be seen in Figure 2.1.

To record a spectrum, the detector signal was recorded before and during the discharge pulses for two intervals totaling 1500 μs. The first interval (750 μs), called a pretrigger interval, was used to record the background laser intensity. The signal during this interval was averaged over time. The second interval contained the absorption signal and was centered around the discharge pulse. The signal recorded in this interval was binned and averaged into 150 five μs intervals. A time-dependent absorbance signal was then calculated by $A = -\ln \frac{I}{I_0}$, where I is the average laser intensity in the bin and I_0 is the time average background laser intensity derived from the pretrigger interval. The resulting absorbance was then averaged for 10 consecutive discharge pulses at which point the laser was stepped by ≈ 0.002 cm^{-1}. This process was

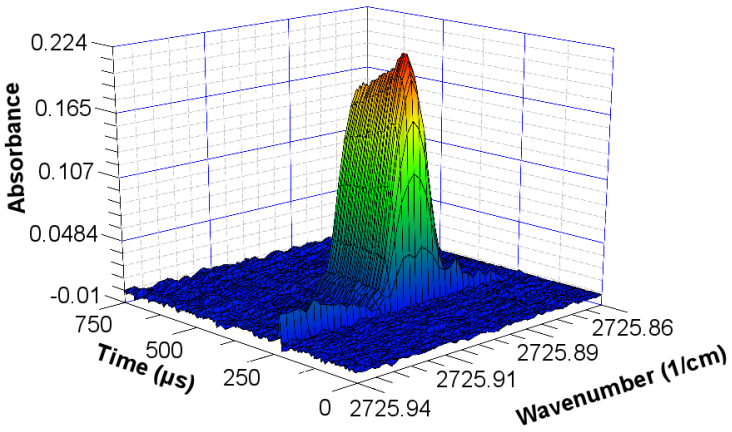

Figure 2.6: An example of a three-dimensional spectrum generated in this experiment. Shown here is the $R(1,0)$ transition of H_3^+ in a n-H_2 plasma cooled with liquid nitrogen. Discharge artifacts were eliminated in this figure to increase clarity. Reproduced from reference [10]

repeated until the full absorption feature was scanned. A three-dimensional spectrum was then generated for each transition studied (See Figure 2.6). Each transition was scanned in triplicate for each set of pressure and temperature conditions.

To analyze the resulting spectrum, the spectrum at each point in time was fitted to a Gaussian function to determine the peak area and linewidth. The kinetic temperature of each line is inferred from the Gaussian linewidth and the average inferred kinetic temperature from all transitions was used as an estimate of the overall plasma kinetic temperature with the standard deviation used as an estimate of the uncertainty. An excitation temperature was calculated from the relative intensities of the two lowest *para* rotational levels (i.e. $\mathrm{R}(1,1)^u$ and the $\mathrm{R}(2,2)^l$) and will be referred to as $T(2,2)$. An additional excitation temperature that was used as a proxy for the rotational temperature and reported as T_{rot}, was also calculated based on the relative intensities of the two levels, $\mathrm{R}(1,1)^u$ and $\mathrm{R}(2,1)^u$. The reason for these two temperatures will be discussed further in Chapter 3.

The final quantity derived from the recorded spectra was p_3, the fraction of p-H_3^+. Using the inferred rotational temperature, T_{rot}, a Boltzmann distribution was calculated for the first 15 levels of o-H_3^+ and p-H_3^+ using the forbidden $(0,0)$ level as a common reference energy. Each manifold was then scaled by the experimentally derived population of the lowest level inferred by the transition intensity (e.g. $\mathrm{R}(1,0)$ for the *ortho* manifold and $\mathrm{R}(1,1)^u$ for the *para* manifold). For each transition measured within the first 15 levels, the calculated population was replaced by the experimentally determined value. p_3 as a function of time was calculated by dividing the sum of all the *para* level populations by the sum of all level populations at each point in time.

Chapter 3

Experimental Results

In this chapter, the experimental results of the investigation aimed at determining the nuclear spin dependence of the $H_3^+ + H_2 \rightarrow H_2 + H_3^+$ reaction (Reaction 1.1) will be discussed. In the first section, measurements that were acquired to ensure sufficient rotational thermalization of the H_3^+ ion generated in a hollow cathode plasma will be presented. In the next section, the potential effect of the three-body reaction, $H_3^+ + 2H_2 \rightarrow H_5^+ + H_2$, as well as provisions taken to understand the influence of three-body collisions on the experimental results, will be discussed. Following this will be a summary of the measurements performed at different temperatures in addition to a section discussing the various models that were employed to derive the experimentally determined hop:exchange ratio, α. Finally, the implications and proposed future directions will be presented. All results discussed in this chapter as well as the reproduced figures have been accepted for publication in the Journal of Chemical Physics and can be found in reference [**?**].

3.1 Thermalization Measurements

In order to validate the measurements to be performed, the degree of thermalization of the rotational levels of H_3^+ generated in the hollow cathode cell had to be evaluated. To accomplish this, the transitions arising from the eight lowest rotational levels within the v_2 fundamental band of H_3^+ were measured in uncooled p-H_2 and n-H_2 plasmas. For each measured transition, a time slice was taken at $t = 300$ μs and was subjected to a Boltzmann analysis. For the uncooled p-H_2 plasma, the kinetic temperature of 337 ± 29 K was found to be in good agreement with *ortho*-H_3^+ rotational temperature of 336 ± 19 K and the *para*-H_3^+ rotational temperature of 316 ± 1 K (Figure 3.1). Similar results were found in an uncooled n-H_2 plasma; the kinetic temperature was 352 ± 29 K, *ortho*-H_3^+ rotational temperature was 339 ± 8 K, and *para*-H_3^+ rotational temperature was 348 ± 13 K. Finally, to demonstrate the same degree of thermalization throughout the pulse, another time slice was taken at $t = 370$ μs and the same analysis was performed with both gases. At this time interval, all plasmas generated in this study demonstrated the same consistency with the calculated temperatures, but at slightly elevated values. This increase in temperature can be attributed to the heating that occurs

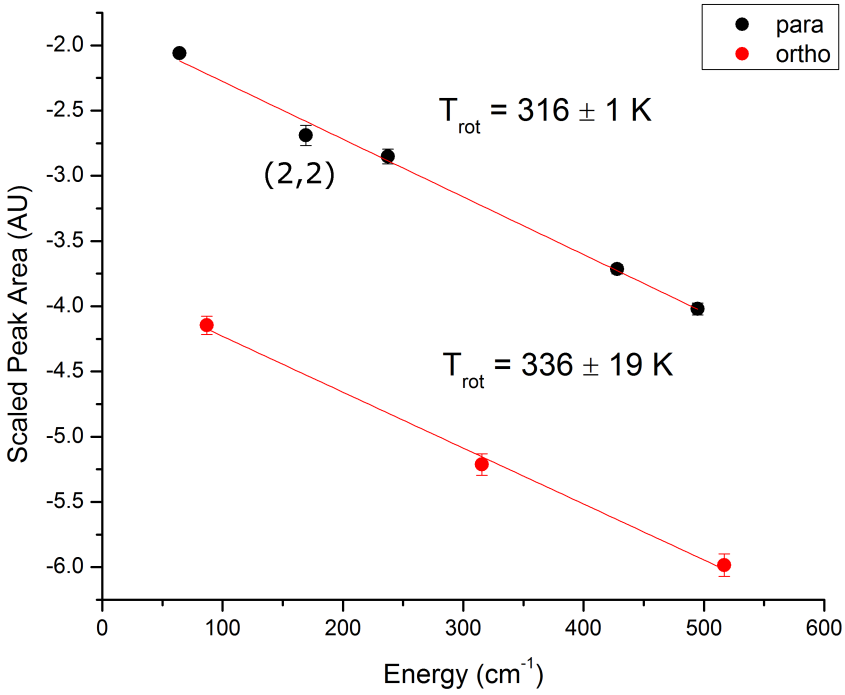

Figure 3.1: Boltzmann plot of an uncooled p-H_2 plasma. The data points were extracted from the time-dependent spectra at $t = 300$ μs. The (2,2) level was excluded from the above fit due to the apparent underpopulation of this level. Upon inclusion of the (2,2) level, the uncertainty in the calculated T_{rot} that is derived from all levels increases.

Table 3.1: T_{kin}, *ortho*-T_{rot}, and *para*-T_{rot} of n-H_2 and *p*-H_2 plasmas generated in an uncooled hollow cathode.

Coolant	Gas	Time (μs)	T_{kin} (K)	*ortho*-T_{rot} (K)	*para*-T_{rot} (K)
Uncooled	*p*-H_2	300	310 ± 33	336 ± 19	316 ± 1
Uncooled	*p*-H_2	370	337 ± 29	339 ± 29	327 ± 1
Uncooled	n-H_2	300	352 ± 29	339 ± 8	348 ± 13
Uncooled	n-H_2	370	361 ± 32	354 ± 5	365 ± 20

during the pulse. A summary of these results can be seen in Table 3.1.

Besides relatively good agreement between the temperatures derived from each rotational manifold as well as the calculated kinetic temperatures, two important observations were made in this study. First, an apparent underpopulation of the (2,2) level was found in all data sets. It was measured significantly and consistently lower than the calculated value obtained from the rotational temperature that is inferred from all other measured rotational levels (Figure 3.1). Also, it was found that the signal-to-noise ratio of the $R(3,3)^l$ transition observed in a liquid-nitrogen-cooled plasma was low. This is an expected result of the depopulation of the (3,3) level at lower temperatures. Since the above thermalization measurements found that the *ortho*-H_3^+ rotational temperature was consistent with the *para*-H_3^+ rotational temperature as well as observing the underpopulation of the (2,2) level, the (1,1) and (2,1) levels, the lowest and third lowest *para* levels respectively, were used to calculate the rotational temperature for both manifolds, and the subsequently inferred rotational temperatures, T_{rot}, will be calculated using this method.

3.2 Three-Body Effects

When considering the experimental pressures of the hollow cathode cell, it is necessary to evaluate the possible influence of three-body collisions (e.g. $H_3^+ + 2H_2$) and how these additional collisions might affect the experimental determination of the hop:exchange ratio, α. To initially investigate this, the intensity of the $R(1,0)$ transition was measured as a function of cell pressure in a liquid-nitrogen-cooled and uncooled n-H_2 plasma (Figure 3.2). In both plots, the intensity of the $R(1,0)$ transition initially increases with increasing cell pressure. At ~1000 mTorr in the uncooled plasma and ~350 mTorr in the liquid-nitrogen-cooled plasma, the maximum intensity of the $R(1,0)$ transition is observed. After this, the intensity of the $R(1,0)$ transition decreases with increasing pressure. Since the kinetic temperature remains constant over the entire pressure range in both plasmas, the decrease in the $R(1,0)$ transition is not due to a change in the population of the (1,0) level. However, since a constant discharge current was observed with increasing pressure and since the total ion density must be still increasing due to the increase in electron mobility, it is evident that the

H_3^+ ion must be depleted by another chemical process that results in the formation of another stable ion. The most promising conjecture is the formation of the ion species, H_5^+, by the three-body reaction of $H_3^+ + 2H_2$ [31, 53].

To qualitatively assess the influence of three-body collisions in determining α, two sets of measurements were taken in each plasma. For the uncooled measurements, all transitions were measured at 560 mTorr; a pressure that is on the rising edge of the curve where three-body collisions are speculated to be minimal. Transitions were also measured at a higher pressure, 1430 mTorr; a pressure that is on the falling edge of the curve and speculated to be experiencing three-body collisions. This was repeated for the liquid-nitrogen-cooled plasma albeit at lower pressures, 270 and 430 mTorr. The comparison of these data sets aided in identifying the ramifications of three-body collisions in determining the value α of the two-body reaction, reaction 1.1.

3.3 Temperature and p_3 Measurements

Since previous measurements confirmed efficient thermalization of the rotational levels of H_3^+, only the $R(1,1)^u$, $R(1,0)$, $R(2,2)^l$, and $R(2,1)^u$ transitions were recorded. These transitions were recorded in succession at both pressures in a uncooled, liquid-nitrogen-cooled, and heated hollow cathode in order to determine the value of p_3 in a plasma of known *para*-H_2 fraction (referred hereafter as p_2). As stated in Chapter 2, n-H_2 ($p_2 = 0.25$) was used directly from the hydrogen generator, and the p-H_2 ($p_2 = 0.999$) was used directly from the *para*-hydrogen converter. Finally, all other mixtures were made in advance to ensure the mixture was evenly blended.

3.3.1 Uncooled Measurements

Measured integrated intensities of each transition, the derived temperatures, and p_3 are reported in Table 3.2 and Table 3.3. For both pressures, p_3 is plotted against p_2 and an increase in p_3 with the corresponding increase in p_2 is observed (Figure 3.3). Only minor differences between the two pressures are observed and this is indicative that the effect of three-body collisions is minimal at this temperature. In order to confirm this suspicion, modeling of reaction 1.1 is needed and will be discussed in Section 3.4. Finally, the kinetic, rotational, and $T(2,2)$ temperatures are plotted versus p_2 (Figure 3.4). Temperatures are similar among the various p_2 mixtures with the following variance-weighted means: $T_{kin} = 351 \pm 10$ K, $T_{rot} = 310 \pm 8$ K, and $T(2,2) = 187 \pm 5$ K. $T(2,2)$, however, is found to be consistently lower than the derived kinetic and rotational temperature. This is suggestive of the apparent depopulation of (2,2) level as mentioned in the

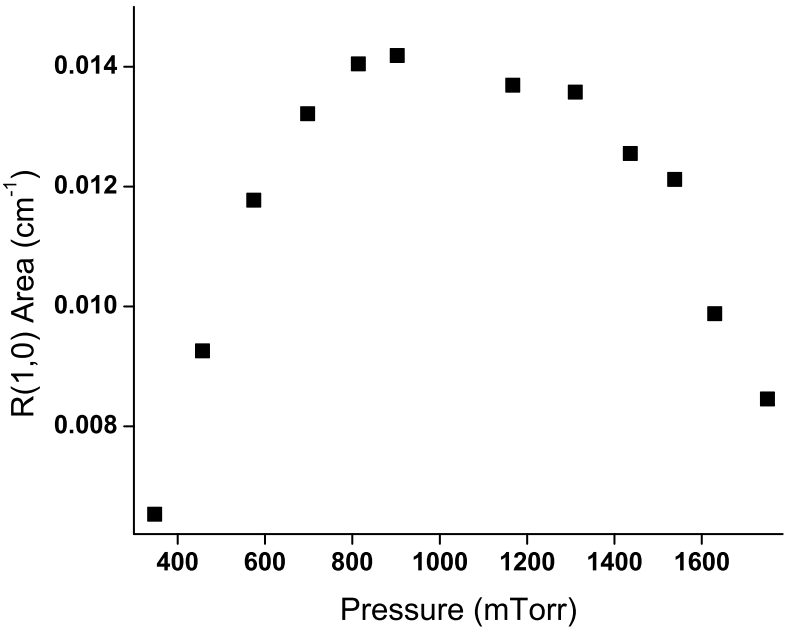

(a) Uncooled n-H_2 plasma.

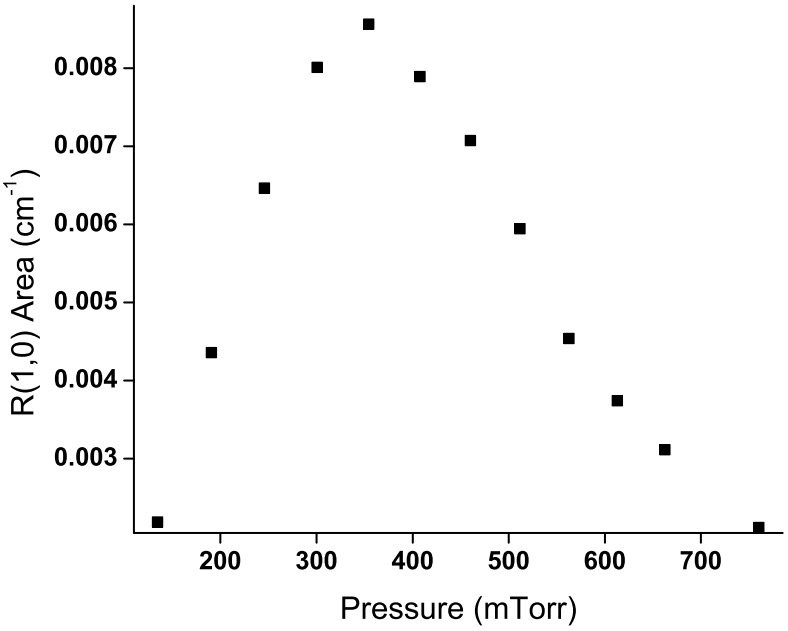

(b) Liquid-nitrogen-cooled n-H_2 plasma.

Figure 3.2: $R(1,0)$ integrated peak area taken at $t = 300$ μs as a function of cell pressure in both an uncooled and liquid-nitrogen-cooled n-H_2 plasma.

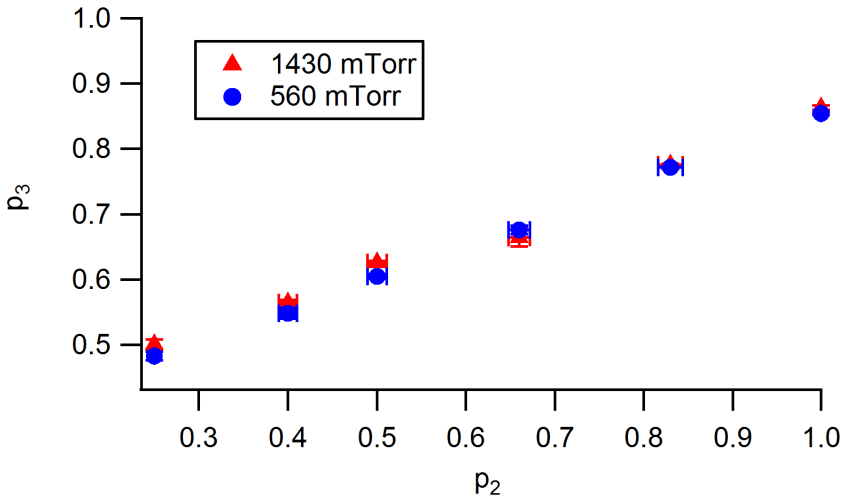

Figure 3.3: Experimental measurements of p_3 plotted against p_2 for an uncooled hollow cathode at pressures 560 and 1430 mTorr.

previous section.

3.3.2 Liquid-Nitrogen-Cooled Measurements

All measurements including integrated intensities of each transition, rotational and kinetic temperatures, and p_3 are reported in Table 3.4 and Table 3.5. Like the uncooled measurements, transitions were recorded at two pressures and p_3 was plotted against p_2. Although there was not a significant difference between the two pressures at high temperatures, the p_3 versus p_2 plot indicates that three-body collisions might play a larger role at this lower temperature (Figure 3.5). Again, modeling of reaction 1.1 is needed to confirm this claim and will be further discussed in Section 3.4.

Another interesting result from the liquid-nitrogen-cooled measurements is the calculated temperatures as seen in the resulting plot of temperatures versus p_2 (Figure 3.6). Similar to the uncooled data, the kinetic temperature remains constant with increasing p_2 with a variance-weighted mean of 139 ± 4 K for 270 mTorr data set and 136 ± 5 K for the 430 mTorr data set. Both T_{rot} and $T(2,2)$, however, do not remain constant, but rather decrease with increasing p_2. This observation could be explained by the higher energy levels of p-H_3^+ being selectively destroyed at a faster rate as p_2 increases. Despite not observing the (3,3) level of o-H_3^+ in this set of measurements, previous thermalization measurements do not support the speculation of *para* levels being selectively destroyed. Finally, $T(2,2)$ is consistently lower than T_{rot}, and it is indicative of the apparent depopulation of the $(2,2)$ level as discussed previously.

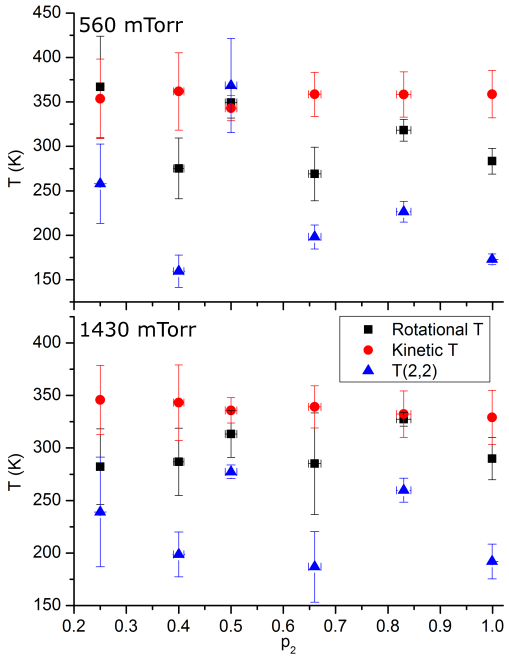

Figure 3.4: Calculated kinetic and rotational temperatures and the quantity $T(2,2)$ plotted against p_2 for both pressures measured in an uncooled hollow cathode.

Table 3.2: Calculated kinetic and rotational temperatures and p_3. Numbers in parentheses represent 1σ uncertainty in the final digit(s).

Pressure (mTorr)	p_2	T_{kin} (K)	T_{rot} (K)	p_3
560	0.25	354(45)	367(57)	0.483(7)
	0.40	362(44)	275(34)	0.548(8)
	0.50	343(14)	349(17)	0.605(4)
	0.66	359(25)	269(30)	0.676(7)
	0.83	358(25)	318(12)	0.772(1)
	0.999	359(27)	283(15)	0.855(2)
1430	0.25	346(33)	282(36)	.501(7)
	0.40	343(36)	287(32)	0.564(4)
	0.50	336(12)	313(22)	0.626(4)
	0.66	339(20)	285(48)	0.665(14)
	0.83	332(22)	327(7)	0.775(2)
	0.99	329(26)	290(20)	0.863(3)

Table 3.3: Integrated intensities of the transitions from the four lowest rotational states of H_3^+ in an uncooled hollow cathode of varying p_2. Numbers in parentheses represent 1σ uncertainty in the final digit(s).

Pressure (mTorr)	p_2	$R(1,1)^u$ 10^{-3} cm^{-1}	$R(1,0)$ 10^{-3} cm^{-1}	$R(2,2)^l$ 10^{-3} cm^{-1}	$R(2,1)^u$ 10^{-3} cm^{-1}
560	0.25	4.92(46)	15.2(4)	5.11(21)	4.79(24)
	0.40	7.87(65)	17.3(8)	5.69(39)	6.11(47)
	0.50	4.73(16)	9.22(35)	5.86(28)	4.45(3)
	0.66	9.79(40)	13.0(7)	8.52(28)	7.44(71)
	0.83	6.46(18)	5.41(41)	6.18(13)	5.67(7)
	0.999	9.93(20)	4.58(27)	7.73(18)	7.91(32)
1430	0.25	5.18(55)	14.7(5)	5.13(46)	4.11(16)
	0.40	7.08(47)	15.1(13)	6.17(28)	5.70(39)
	0.50	5.97(3)	10.4(6)	6.46(8)	5.17(29)
	0.66	8.18(87)	11.3(5)	6.79(68)	6.55(68)
	0.83	7.87(10)	6.57(7)	8.21(8)	7.06(5)
	0.99	10.1(3)	4.41(30)	8.58(53)	8.22(43)

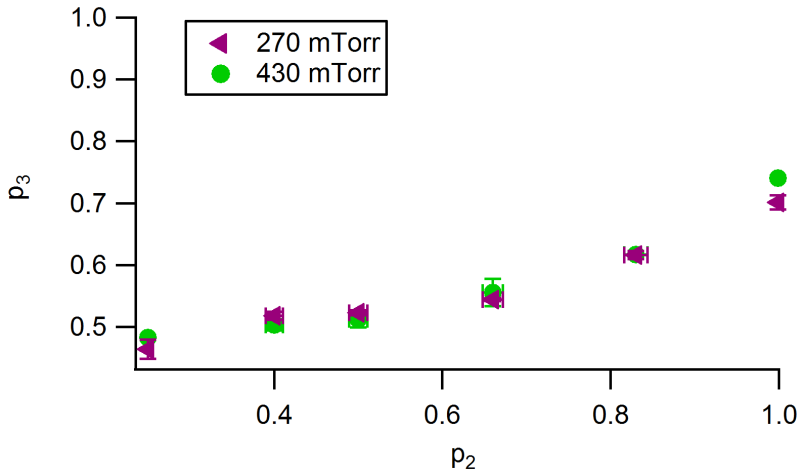

Figure 3.5: Experimental measurements of p_3 plotted against p_2 for a liquid-nitrogen-cooled hollow cathode at pressures 270 and 430 mTorr.

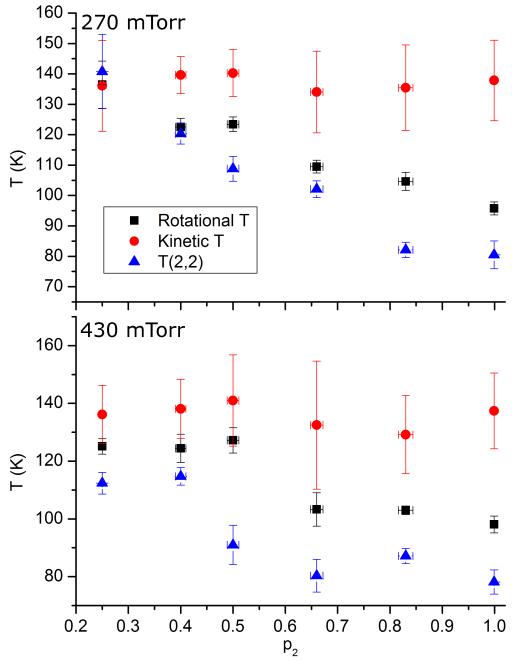

Figure 3.6: Calculated kinetic and rotational temperatures and the quantity $T(2,2)$ plotted against p_2 for an liquid-nitrogen-cooled hollow cathode at both pressures.

Table 3.4: Calculated kinetic and rotational temperatures and p_3 for a given p_2 studied in a liquid-nitrogen-cooled hollow cathode. Numbers in parentheses represent 1σ uncertainty in the final digit(s).

Pressure (mTorr)	p_2	T_{kin} (K)	T_{rot} (K)	p_3
270	0.25	136(15)	136(8)	0.464(16)
	0.40	140(6)	123(3)	0.518(6)
	0.50	140(8)	123(2)	0.523(4)
	0.66	134(13)	110(2)	0.544(3)
	0.83	135(14)	105(3)	0.616(6)
	0.999	138(13)	96(2)	0.701(11)
430	0.25	136(10)	125(3)	.483(4)
	0.40	138(10)	124(5)	0.503(9)
	0.50	141(16)	127(5)	0.512(13)
	0.66	132(22)	103(6)	0.556(22)
	0.83	129(14)	103(1)	0.617(1)
	0.99	137(13)	98(3)	0.741(1)

Table 3.5: Integrated intensities of the measured transitions in an liquid-nitrogen-cooled hollow cathode of varying p_2. Numbers in parentheses represent 1σ uncertainty in the final digit(s).

Pressure (mTorr)	p_2	$R(1,1)^u$ 10^{-3} cm^{-1}	$R(1,0)$ 10^{-3} cm^{-1}	$R(2,2)^l$ 10^{-3} cm^{-1}	$R(2,1)^u$ 10^{-3} cm^{-1}
270	0.25	9.11(82)	127.1(9)	5.81(15)	2.82(15)
	0.40	13.8(4)	31.6(5)	7.36(12)	3.48(12)
	0.50	15.2(5)	32.7(11)	7.04(28)	3.86(7)
	0.66	14.2(5)	27.5(14)	6.03(13)	2.08(8)
	0.83	18.2(5)	24.3(5)	5.39(26)	3.23(20)
	0.999	20.2(9)	18.3(2)	5.77(56)	2.88(10)
430	0.25	9.82(25)	25.2(6)	4.77(18)	2.57(9)
	0.40	8.78(21)	20.9(12)	4.39(11)	2.27(17)
	0.50	9.77(46)	20.8(6)	3.46(40)	2.64(13)
	0.66	10.6(8)	18.0(8)	3.01(31)	1.82(19)
	0.83	9.31(8)	12.6(3)	3.06(16)	1.59(5)
	0.99	10.4(4)	7.63(65)	2.80(27)	1.57(10)

3.3.3 Heated Measurements

A final temperature measurement was taken at an elevated temperature in order to verify the trend of α with the temperature of the plasma. As mentioned in the previous chapter, a fluid circulator was used to heat and circulate ethylene glycol at 100°C. All four transitions were recorded in a 99.9 % p-H_2 plasma and had a calculated kinetic temperature of 450 ± 75 K. p_3 was also determined to be 0.883 ± 0.007.

3.4 Modeling

In order to extract the value of α from the experimental data, steady state modeling was performed by Kyle N. Crabtree. The derived models were adapted from previous modeling on reaction 1.1 by former graduate student, Brian A. Tom [60]. In these models, referred to as the high and low temperature models, p_3 is calculated as a function of p_2 and α. The key assumption in both these models is that the *ortho:para* ratio of H_3^+ is governed by reaction 1.1. This assumption is satisfied in these experimental conditions if steady state of reaction 1.1 has been reached before the H_3^+ ion is destroyed by electron recombination. Given that reaction 1.1 is estimated to be at steady state within a few reactive collisions [11] and the reactant H_3^+ will experience an order of magnitude more collisions with the buffer gas of H_2 than electrons, the assumption is valid in the current experimental conditions. Each model is discussed briefly and the results of these models with respect to the experimental measurements are summarized here. Full details of these models can be found elsewhere [11].

3.4.1 High Temperature Model

Model

At higher temperatures as in an uncooled plasma, it is further assumed that the outcome of reaction 1.1 is entirely governed by the nuclear spin statistical weights as outlined in Chapter 1. Since there is sufficient energy to access a large number of rotational levels, this assumption is reasonable given the temperatures in the uncooled and heated measurements. Equation 3.1 is the resulting formula that expresses the quantity p_3 as a function of both p_2 and α. The equation results in a straight line that passes through an assumed point for a n-H_2 plasma (p_3, p_2 = 0.5, 0.25), and has a slope that is related to the quantity α.

$$p_3 = \frac{\alpha + 2\alpha p_2 + 1}{3\alpha + 2} \tag{3.1}$$

In order to investigate the effect of three-body collisions from the reaction $H_3^+ + 2H_2$ as discussed in Section 3.2, the two-body model was modified to incorporate three-body collisions that result in a change in nuclear spin. The additional assumption in this model is that the reaction leading to the formation of the stable H_5^+ does not ultimately affect the p-H_3^+ fraction. Equation 3.2 is the resulting equation that includes these effects where α_2 is the same α from equation 3.1, α_3 is the three-body hop:exchange ratio, and Φ_2 is the branching fraction of reactive two-body collisions compared to reactive three-body collisions.

$$p_3 = \frac{\frac{\Phi_2}{1+\alpha_2}\left(\frac{\alpha_2}{3} + \frac{2\alpha_2 p_2}{3} + \frac{1}{3}\right) + \frac{1-\Phi_2}{1+\alpha_3}\left(\frac{39\alpha_3}{100} + \frac{13\alpha_3 p_2}{50} + \frac{19}{50} + \frac{3p_2}{25}\right)}{\frac{\Phi_2}{1+\alpha_2}\left(\alpha_2 + \frac{2}{3}\right) + \frac{1-\Phi_2}{1+\alpha_3}\left(\frac{91\alpha_3}{100} + \frac{41}{50}\right)} \tag{3.2}$$

With this model, Crabtree *et al.* performed several simulations to facilitate insight into the extent to which three-body collisions affect the determination of α [11]. In these simulations, it was observed that if α_3 is large, the slope of the generated curves would be more shallow . Furthermore, the effect of Φ_2 term was investigated. In general, Φ_2 is expected to decrease with an increase in H_2 number density (i.e. as three-body collisions become more important), and as a result the slope of the generated curves becomes more shallow. Therefore, if three-body collisions are important, the slope of the measurements taken at higher pressure will be less than the slope of the measurements taken at lower pressures. In general, these trends indicate that if three-body effects are important in the experimental results and the two-body model is used, an underestimation of α will result.

Uncooled Data Results

As seen in Figure 3.7, the data agree reasonably well with the two-body model and indicate that three-body collisions do not seem to influence the experimental measurements. However, it is observed that the low

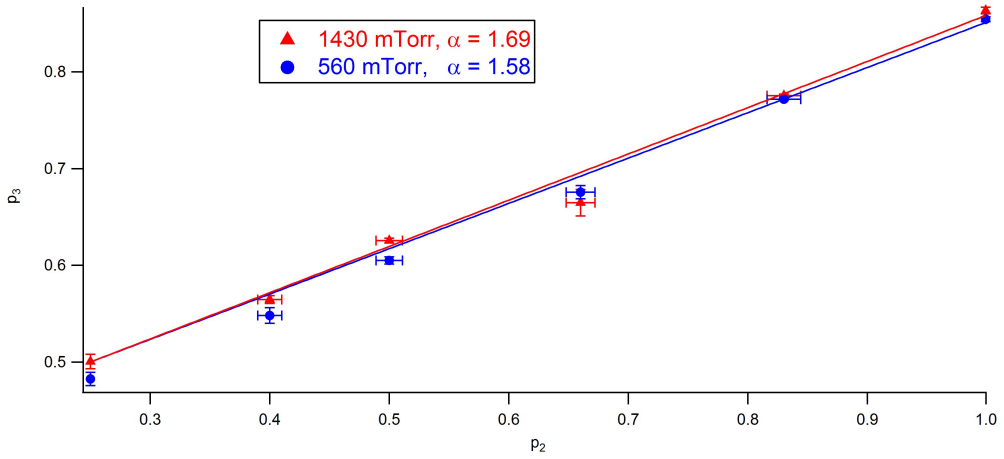

Figure 3.7: High temperature model fitted to experimental measurements performed in an uncooled plasma.

pressure data which is assumed to be minimally experiencing three-body collisions are consistently lower than the simulated curve from the two-body high temperature model. Since it is postulated that three-body collisions do not affect the measurement of p_3 and thus the determination of α at this pressure, it is believed that the resulting trend is more similar to the curves produced by the low temperature model to be discussed in the next section. As a result, it is postulated that even at higher temperatures (350 K), energetic effects may still restrict some of the possible product channels. Regardless, the generated curves from the two-body high temperature model agree with the experimental data and result in $\alpha = 1.58 \pm 0.02$ for the 560 mTorr data set and $\alpha = 1.69 \pm 0.03$ for the 1430 mTorr data set.

These results can be compared to a similar measurement of reaction 1.1 that was performed in a pulsed hollow cathode by Cordonnier *et al.* [8] In their study, they measured the ratio of the peak intensities of the $R(1,0)$ and $R(1,1)^u$ transitions in a n-H_2 and p-H_2 plasma at a pressure of 1.85 Torr and a temperature of approximately 400 K. From their experimental results, they derived $\alpha = 2.4 \pm 0.6$. The α inferred from our model falls right below the uncertainty of their derived value. Since α is expected to decrease with decreasing temperature [60], it speculated that this descrepancy is due to the temperature differences between the two experiments. Regardless of this discrepancy, their results can be used to validate the two-body high temperature model. Using their measured values of $p_3 = 0.893$ at $p_2 = 0.999$ in combination with our derived two-body high temperature model (Equation 3.1) results in a similar value of $\alpha = 2.46$. Clearly, this comparison validates the two-body high temperature model used in this study.

In addition to comparing the derived α with Cordonnier *et al.*, it is also important to address the discussed issue of back conversion of p-H_2 to o-H_2 that they observed in their plasma over the course of the discharge pulse and demonstrated in their Figure 2. Plotting our results in a similar format shows similar

time-dependent behavior in the 1430 mTorr data set, i.e. a slow rise of the H_3^+ absorption and a slight increase in the $R(1,0)$ peak area over time in a p-H_2 plasma (Figure 3.8). This issue is not observed in the 560 mTorr data set. The difference between these two measurements could be due to the higher ion density in the 1430 mTorr data set and as a result, promotes more H atom recombination on the walls of the cathode. The net effect of this process results in the formation of n-H_2 in the standard $3:1$ *ortho:para* ratio and over time, can be produced in large enough quantities to affect the overall p-H_2 fraction. However, this study observed this process at lesser extent than the work of Cordonnier *et al.* Since their study is also at higher pressures, it is likely that this is the cause of making this effect more pronounced. Regardless, the derived α in this work was based on measurements taken early in the discharge pulse where the effects of H atom recombination are thought to be minimal.

Finally, a similiar study on the reaction of D_3^+ with H_2 was performed in an ion trap by D. Gerlich in 1993 [24]. In this study, α was determined to be 1.6 at 44 meV. This approximately corresponds to a temperature of 340 K which is in excellent agreement with our inferred value of α.

Heated Data Results

Using the measured p_3 at $p_2 = 0.999$ and the two-body high temperature model, α was determined to be 2.2 ± 0.3. Despite only obtaining one measurement at this temperature, the measured p_3 and the derived α was signfigantly higher than in the uncooled data set. This result is consistent with an increase in α with an increase in temperature [60].

3.4.2 Low Temperature Model

Model

At lower temperatures, it is no longer valid to assume that the outcome of reaction 1.1 is entirely governed by the nuclear spin statistical weights. Instead, it is assumed that at lower temperatures, energetics need to be incorporated into the model. To illustrate this idea, consider the process of converting p-H_3^+ to o-H_3^+. This requires 170 K of energy, and therefore, this product channel is not favorable with the temperatures of the liquid-nitrogen-cooled measurements. To include these energetic considerations, a new model known as the low temperature model was derived (Equation 3.3) [11]. In this model rate coefficients are annotated as k_{ijkl} to represent the rate coefficients of the reactions in the form i-$H_3^+ + j$-$H_2 \rightarrow k$-$H_3^+ + l$-H_2 are included. For example, k_{poop} represents the rate coefficients for the reaction of p-$H_3^+ + o$-$H_2 \rightarrow o$-$H_3^+ + p$-H_2. Each of these coefficients depends upon T_{kin}, T_{rot}, and the branching fractions for the identity, hop, and exchange reactions (S^{id}, S^{hop}, and S^{exch} respectively, where the formerly defined $\alpha = S^{hop}/S^{exch}$). All coefficients

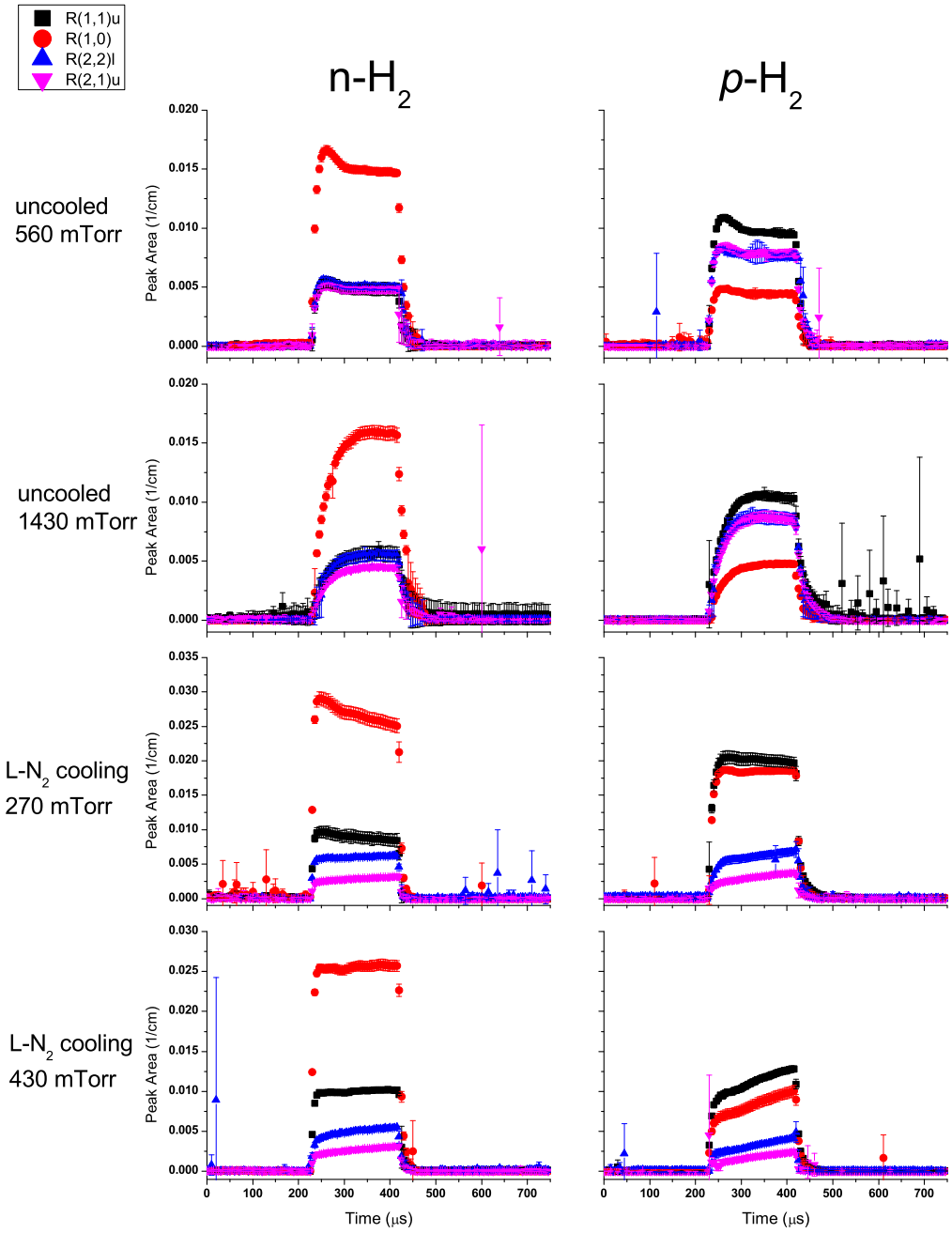

Figure 3.8: Time-dependence of integrated intensities of all transitions studied in n-H_2 and p-H_2 uncooled and liquid-nitrogen-cooled plasmas. Non-zero peaks areas outside of the pulse is due to Gaussian fits to a noise feature in the spectrum. A slight increase in the $R(1,0)$ peak area over time in the p-H_2 plasma was observed and this is postulated to be due to H-atom recombination on the walls of the cathode.

were calculated using the microcanonical statistical model of Park and Light [42].

$$p_3 = \frac{(k_{oopp} + k_{oopo})(1 - p_2) + k_{oppo}p_2}{(k_{oopp} + k_{oopo} + k_{poop} + k_{pooo})(1 - p_2) + (k_{oppo} + k_{ppoo})p_2} \tag{3.3}$$

Further modification of this model to include three-body effects as previously done with the high temperature model were not performed due to the large number of unknown rate coefficients of the three-body reactions. Therefore, no prediction of how three-body collisions affect the p_3 vs. p_2 can be made . However, it is known that the rates of ternary association reactions that result in the formation of H_{2n+1} clusters increase with decreasing temperatures [31, 44]. It can not be concluded if this process has any dependence on the nuclear spin configuration of the precursor ion, H_3^+. However, it is found that this rate is dependent on the nuclear spin configuration of H_2, and specifically, Paul *et al.* found that the rate coefficient with *p*-H_2 is an order of magnitude faster than with n-H_2 at 10 K [44].

In order to fit the experimental results, rate coefficients were calculated and the model was used to simulate a variety of conditions. The parameters were set as follows: S^{id} was set to the statistical value of 0.1, α was set to $0, 0.1, 0.5, 2, 10$, and ∞, T_{kin} was 135 K from the experimental value, and T_{rot} was varied in the range of 85 to 145 in steps of 5 K. The resulting p_3 vs. p_2 curves were plotted with experimental values as seen in Figure 3.9. The 270 mTorr data set agrees well with the curves generated with $\alpha = 0.5$ regardless of the value of T_{rot}. Since the curvature changes minimally with changing values of T_{rot}, the change in the parameter α is a more important effectto observe in order to show agreement with the experimental data as seen in the lower plot of Figure 3.9. The 430 mTorr data set does not fit well with any of the calculated curves and is most likely due to three-body effects. This is a reasonable conjecture due to the previous discussion on the increase in the rate of ternary association reactions with a decrease in temperature reported in the literature [31, 44]. As a result, no value of α is assigned. Conversely, the low pressure data for a plasma at 139 ± 4 K is reported with an $\alpha = 0.5 \pm 0.1$. This statistical result suggests that even at this temperature, the lifetime of the intermediate complex, H_5^+, is sufficient for full proton scrambling.

3.5 Concluding Remarks

The nuclear spin dependence of the reaction of H_3^+ with H_2 has been investigated by measuring the four lowest rotational levels of H_3^+ in various *para*-enrichments of H_2 plasmas at various temperatures. By combining steady-state modeling with experimental measurements, the ratio of the hop to exchange reaction, α, has been inferred to be 1.6 ± 0.1 at 350 K and for the first time at lower temperatures, 0.5 ± 0.1 at 135 K. Preliminary measurements at 450 K were also measured and resulted in an inferred α value of 2.2 ± 0.3. All

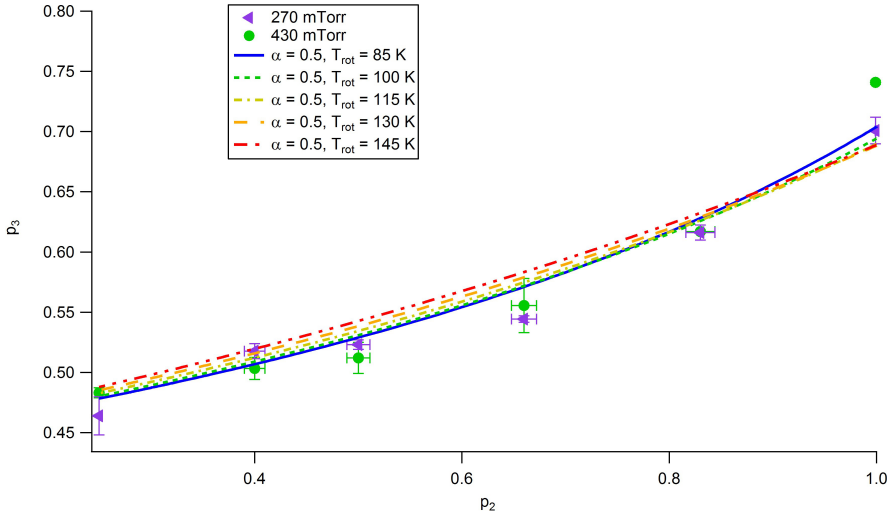

(a) The parameter T_{rot} is varied while α, S^{id}, and T_{kin} are held constant.

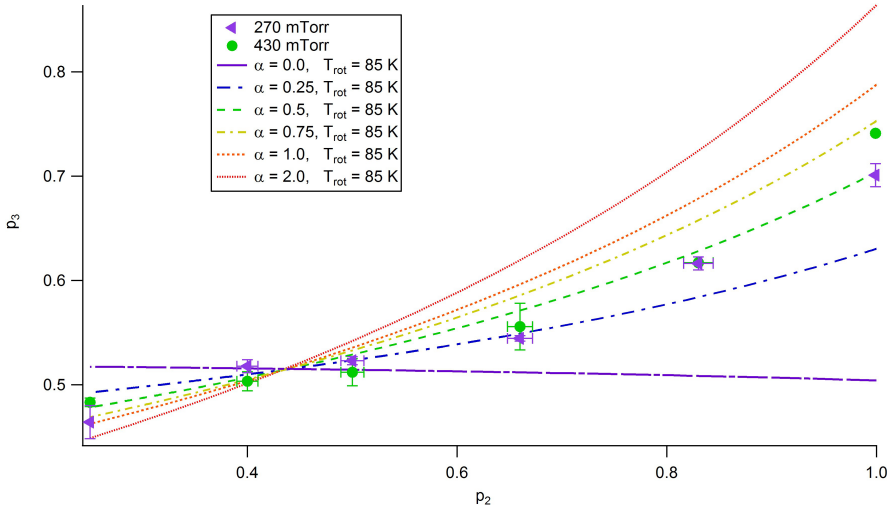

(b) The parameter α is varied while T_{rot}, S^{id}, and T_{kin} are held constant.

Figure 3.9: Liquid-nitrogen-cooled data and the generated low temperature model curves.

results coincided with previous measurements of this reaction at 400 K by Cordonnier *et al.* [8] as well as measurements of the analogous deuterated system studied by Gerlich *et al.* [24]

In the efforts to determine α of reaction 1.1, experimental complexities became apparent. The consistent underpopulation of (2,2) level relative to all other levels measured in the plasma has been encountered in addition to an apparent trend of the rotational temperature of H_3^+ decreasing with the corresponding increase in p-H_2 fraction (p_2) at liquid-nitrogen-cooled temperatures. It is unclear whether these observations are due to ternary reactions occurring in the plasmas generated in these studies or the fact that state-selective processes are occurring. In order to clarify these observations, a collaborative investigation of this reaction in an ion trap is planned for the near future. These measurements will not only eliminate ternary reactions by reducing the gas density, but will also allow measurements at even lower and more astrophysically relevant temperatures. These additional measurements in combination with establishing a new collaboration to acquire fully quantum reactive scattering calculations on the H_5^+ potential energy surface will allow us further insight into this reaction and brings us one step closer to using H_3^+ as a useful temperature probe of the interstellar medium.

Chapter 4

The Elusive HO_2^+ Ion

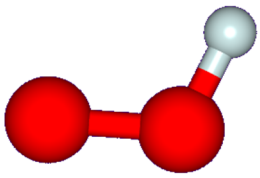

Figure 4.1: The HO_2^+ molecular ion.

In 1984, it was reported that less than 1% of the most common polyatomic molecular ions have a corresponding high resolution spectrum [51]. This low percentage is due to the many difficulties encountered in high resolution spectroscopy of gas-phase polyatomic molecular ions. This includes producing a significant concentration of the desired ion and having the capability to distinguish the generated ions from neutrals. In addition to this low percentage, most of the observed ions are protonated neutral diatomics. Yet, protonated oxygen, also known as the HO_2^+ ion, has still eluded numerous scientists in the search for the high resolution spectrum of this species.

Besides its elusive character, HO_2^+ plays an important role in many areas of biology, chemistry, and astronomy. Like many molecular ions, it is proposed that this molecular ion serves as an important reaction intermediate in various organic reactions [13]. It also holds an important role in biological processes (e.g. respiration), oxidation processes, radiation chemistry, H_2/O_2 fuel cells, flame, and plasma chemistry [46, 13, 52]. Finally, similar to the H_3^+ ion as discussed in previous chapters, HO_2^+ has been reported to be an astronomical species residing in interstellar clouds, comet tails, and planetary atmospheres [13].

$$H_3^+ + O_2 \rightleftharpoons HO_2^+ + H_2 \tag{4.1}$$

The HO_2^+ ion is speculated to form in the interstellar medium and in laboratory plasmas via the reaction 4.1 [26, 66]. Given that H_3^+ is a very efficient protonator as well as a dominant ion residing in the interstellar clouds, reaction 4.1 is likely the primary means by which HO_2^+ is generated in interstellar clouds. Recent

calculations suggest that this reaction is slightly endothermic by 50 ± 9 cm^{-1} and have yielded an estimated number density of $n(HO_2^+) \approx 7 \times 10^{-10}$ cm^{-3} in interstellar clouds [66]. This number density is below the detection limit of current radiotelescope receivers, but future technology could potentially make this species a viable tracer for the problematic O_2 molecule [26, 66].

In this chapter, an experimental search for the HO_2^+ ion is discussed. First, a brief review of previous theoretical and experimental work is presented. Although reaction 4.1 is the dominant means by which the HO_2^+ ion is generated in the interstellar medium, other formation and destruction pathways that occur in a laboratory plasma must also be examined. Finally, a proposed investigation is outlined and includes gas mixture ratios to investigate as well as a proposed frequency scanning range.

4.1 Previous Work

Previous work on the HO_2^+ molecular ion spans over three decades with most work involving theoretical calculations of the fundamental vibrational modes. The first study was that of van Lenthe and Ruttink, who used the self-consistent-field method to theoretically calculate the equilibrium geometries of the three lowest electronic states: $^3A''$, $^1A'$, and $^1A''$ [33]. Although no vibrational frequencies were predicted, this study was shortly followed by a direct experimental investigation by Dyke *et al.* using vacuum ultraviolet photoelectron spectroscopy [16]. In this work, Dyke and coworkers derived the adiabatic ionization potential (IP) of the neutral molecule HO_2 and were able to improve the value for the heat of formation of HO_2^+ as well as the proton affinity of the neutral O_2 molecule. Most importantly, Dyke *et al.* theoretically calculated the vertical IP's of HO_2 and derived vibrational frequencies using the derived force constants from van Lenthe and Ruttink. They reported the following frequencies (cm^{-1}) of three fundamental vibrational modes: $\nu_1 = 3577$, $\nu_2 = 1576$, and $\nu_3 = 1346$.

Although these values are quite far off from the current predicted values, this study stimulated additional studies on this elusive ion. In 1983, Raine *et al.* obtained vibrational frequencies by direct quantum mechanical treatment of the vibration-rotation energy levels [51]. Their derived frequencies (cm^{-1}) are as follows: $\nu_1 = 3200$, $\nu_2 = 1570$, and $\nu_3 = 1150$. In order to validate their calculations, Raine *et al.* applied their method to previously measured vibrational frequencies of HN_2^+ and HCO_2^+, and found relatively good agreement between their calculated values and measured values. Shortly after, DeFrees *et al.* performed *ab initio* calculations of this ion yielding similar results as Raine *et al.* and the frequencies (cm^{-1}) are as follows: $\nu_1 = 3204$, $\nu_2 = 1572$, and $\nu_3 = 1144$. Finally, in 1989, the variational work of Quelch *et al.* yielded slightly lower frequencies (cm^{-1}) [46] and are as follows: $\nu_1 = 3140$, $\nu_2 = 1535$, and $\nu_3 = 1140$.

After nearly a decade of theoretical efforts to assist laboratory experiments, no detection of HO_2^+ was reported and no additional scientific work was reported on this species for nearly another decade. Then in 1997, Nizkorodov and coworkers revived the search with photodissociation spectroscopy [39]. In this work, He and Ne tagged HO_2^+ ions were generated, and the ν_1 of bare HO_2^+ was estimated to be significantly lower at approximately $3020 \pm 40 cm^{-1}$. Even with a continually decreasing trend of the vibrational frequencies, another calculation was performed by Robbe *et al.* in 2000 and showed significantly different frequencies (cm^{-1}) as follows [52]: $\nu_1 = 3268.25$, $\nu_2 = 1392.45$, and $\nu_3 = 1113.65$. Despite these derived values, a more recent work produced much lower frequencies (cm^{-1}) that were similar to the photodissociation studies [66]: $\nu_1 = 3028$, $\nu_2 = 1440$, and $\nu_3 = 1068$.

With a rather broad range of frequencies derived from theory, it not surprising that this ion has yet to be experimentally detected. In 1991, an experimental attempt at observing the ν_1 fundamental mode of HO_2^+ by the Oka Group in Chicago was reported. In this study, they covered a broad range of frequencies, 3250-3600 cm^{-1}, with a 1:1 ratio of H_2:O_2 [27]. Although unsuccessful at observing HO_2^+, they were able to observe and analyze the H_3O^+ ion. There are numerous possibilities as to why they failed to detect HO_2^+, but two obvious speculations can be formed; either they did not generate enough HO_2^+ or they were scanning in the wrong frequency range. Given that most of the theoretical work has converged to the 3000 cm^{-1} region (See Figure 4.2), it is most likely that they were in the wrong frequency range. Thus, this renews hope that given the right plasma conditions and a lower scanning range, detection of HO_2^+ is still possible.

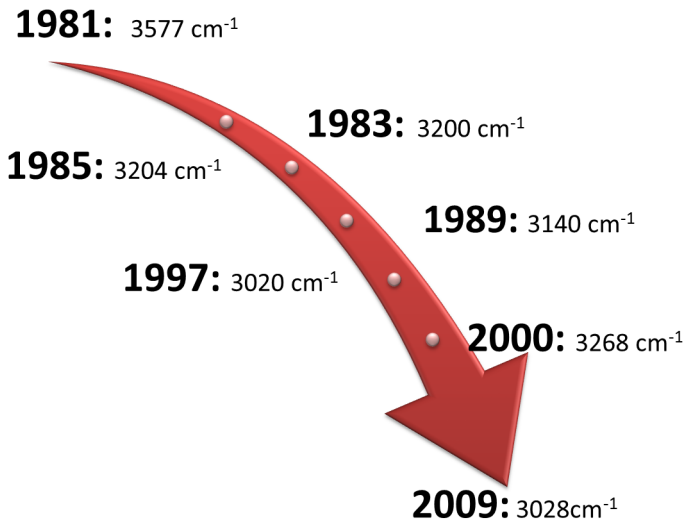

Figure 4.2: Timeline of the predicted frequency of the ν_1 mode of HO_2^+

4.2 Plasma Chemistry

In order to ensure detection of HO_2^+, an analysis of the plasma chemistry and an expected signal-to-noise calculation is needed. The primary formation and destruction reaction of the HO_2^+ ion in the interstellar medium has previously been stated as reaction 4.1. In a laboratory plasma, HO_2^+ can also be formed by a proton transfer between H_2^+ and O_2 (reaction 4.2). Reaction 4.2 is in direct competition with the reaction between H_2^+ and H_2 to form H_3^+, and therefore, it is necessary to include this reaction in addition to reaction 4.1.

$$H_2^+ + O_2 \rightarrow HO_2^+ + H \tag{4.2}$$

$$H_2O + HO_2^+ \rightarrow O_2 + H_3O^+ \tag{4.3}$$

$$O + HO_2^+ \rightarrow O_2 + OH^+ \tag{4.4}$$

$$HO_2^+ + e^- \rightarrow O_2 + H \tag{4.5}$$

$$OH + HO_2^+ \rightarrow O_2 + H_2O^+ \tag{4.6}$$

Next, it is important to consider the possible destruction pathways and they are as follows: HO_2^+ reacting with H_2O to form O_2 and H_3O^+ (reaction 4.3), HO_2^+ reacting with atomic oxygen to form O_2 and OH^+ (reaction 4.4), electron recombination of HO_2^+ to form neutral O_2 and atomic hydrogen (reaction 4.5), and HO_2^+ reacting with an OH to form O_2 and H_3O^+ (reaction 4.6). Reactions 4.3 and 4.6 can be neglected if it is assumed that water can be condensed out of the plasma by cooling with liquid nitrogen. Reaction 4.4 can also be ignored since atomic oxygen is not a dominant species occurring in an oxygen-hydrogen plasma [4]. Therefore, reaction 4.5 is the only additional destruction reaction to be included in the estimation of HO_2^+.

In order to include reactions 4.1, 4.2, and 4.5, the number densities of H_2^+ and H_3^+ are required. To calculate these values, the formation and destruction reactions of these species are included. The entire reaction scheme for the formation and destruction of HO_2^+ in a laboratory plasma (4.1, 4.2, and 4.5) including the formation and destruction reactions of H_2^+ and H_3^+ is illustrated in Figure 4.3. Rates constants for all reactions considered in this chemical scheme as well as estimated number densities for 1 Torr of each O_2 and

H_2 can be found in Table 4.1.

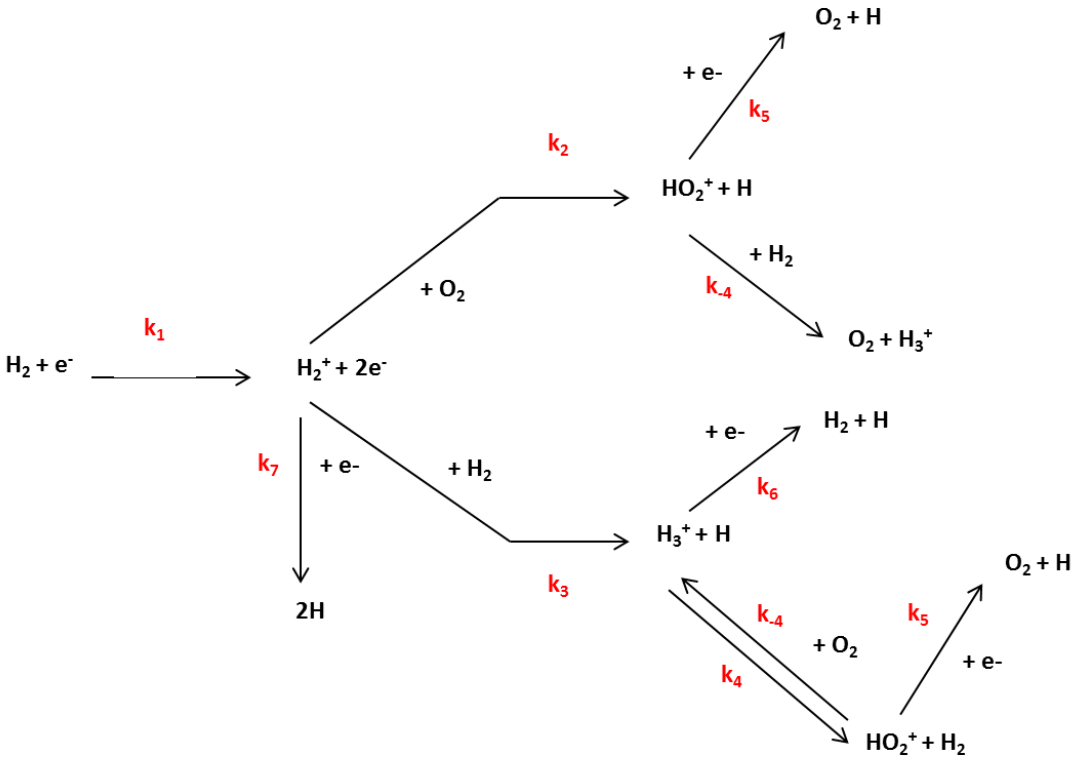

Figure 4.3: Chemical scheme for the formation of HO_2^+ in a laboratory plasma.

Table 4.1: Summary of rate constants and estimated number densities for proposed investigation.

Parameter	Value	Source
k_1	2.5×10^{-11} cm^3 s^{-1}	Reference [8]
k_2	1.9×10^{-9} cm^3 s^{-1}	Reference [68]
k_3	2.1×10^{-9} cm^3 s^{-1}	Reference [68]
k_4	1.5×10^{-9} cm^3 s^{-1}	Reference [68]
k_{-4}	6.4×10^{-10} cm^3 s^{-1}	Reference [68]
k_5	3.0×10^{-7} cm^3 s^{-1}	Reference [68]
k_6	2.3×10^{-8} cm^3 s^{-1}	Reference [68]
k_7	1.6×10^{-8} cm^3 s^{-1}	Reference [68]
$[H_2]$	3×10^{16} cm^3	1 Torr, Ideal Gas Law
$[O_2]$	3×10^{16} cm^3	1 Torr, Ideal Gas Law

Given the above reaction scheme, rate equations can be derived for each ionic species (H_3^+, H_2^+, and HO_2^+). In the case of the H_2^+ ion, it is generated from the electron impact ionization of H_2 and consumed by electron recombination. This species can also react with a neighboring O_2 molecule to form HO_2^+ or with a

neighboring H_2 molecule to form H_3^+. The derived rate equation is then as follows:

$$\frac{\partial[H_2^+]}{\partial t} = k_1[H_2][e^-] - k_2[H_2^+][O_2] - k_3[H_2][H_2^+] - k_7[H_2^+][e^-]$$

For H_3^+, the ion is generated by either the reaction between H_2^+ and H_2 or by the reaction between HO_2^+ and H_2 and is consumed by the reaction between H_3^+ with O_2 to form HO_2^+ or by electron recombination. Including these reactions results in the following rate equation:

$$\frac{\partial[H_3^+]}{\partial t} = k_3[H_2^+][H_2] + k_{-4}[HO_2^+][H_2] - k_4[H_3^+][O_2] - k_6[H_3^+][e^-]$$

The final species is the HO_2^+ ion. The formation is governed by the reaction of H_2^+ with O_2 and H_3^+ with O_2. The destruction terms includes the reaction of HO_2^+ with H_2 and electron recombination. All these terms yield the following rate equation:

$$\frac{\partial[HO_2^+]}{\partial t} = k_2[H_2^+][O_2] + k_4[H_3^+][O_2] - k_{-4}[HO_2^+][H_2] - k_5[HO_2^+][e^-]$$

In order to further simplify these equations, the steady-state approximation is assumed. To validate this assumption, the average number of reactive collisions each ion experiences before being destroyed by electron recombination needs to be considered. The lifetime of each ion is given by $\tau_{life} = (k_{DR}[e^-])^{-1}$. For a positive column discharge, Cordonnier *et al.* report a typical electron density to be on the order 10^{10} cm^{-3} [8]. Since the electron recombination rate for all ions in this scheme are on the order of 10^{-8} cm^3 s^{-1}, $\tau_{life} \approx 10^{-2}$ seconds. Next, the average time between reactive collisions is given by $\tau_{rxn} \approx (k_{rxn}[H_2/O_2])^{-1}$. All formation reaction rates are on the order of 10^{-9} cm^3 s^{-1} and number densities of both H_2 and O_2 are on the order of 10^{16} cm^{-3}. Thus, τ_{rxn} is approximately 10^{-7} seconds. Finally, the average number of reactive collisions each ion experiences before being destroyed by electron recombination is given by τ_{life}/τ_{rxn} and for the above values, yields 10^5 reactive collisions before being destroyed by electron recombination. With such a high number of reactive collisions, the steady-state approximation is proven to be valid. Therefore, the derived expressions that assume steady-state for H_2^+, H_3^+, and HO_2^+ are as follows:

$$[H_2^+] = \frac{k_1[H_2][e^-]}{k_2[O_2] + k_3[H_2] + k_7[e^-]}$$

$$[H_3^+] = \frac{k_3[H_2^+][H_2] + k_{-4}[HO_2^+][H_2]}{k_4[O_2] + k_6[e^-]}$$

$$[HO_2^+] = \frac{k_2[H_2^+][O_2] + k_4[H_3^+][O_2]}{k_{-4}[H_2] + k_5[e^-]}$$

It can be further assumed that at steady-state the rate at which H_2^+ is formed by electron impact ionization of H_2 must be equal to the rate at which all ions are destroyed by electron recombination ($k_1[H_2][e^-] = k_5[HO_2^+][e^-] + k_6[H_3^+][e^-] + k_7[H_2^+][e^-]$). Since the electron recombination rates for all ions are approximately the same value ($k_5 \approx k_6 \approx k_7$), a unified electron recombination rate, k_{DR} is assumed for all ions and the previous equation is simplified ($k_1[H_2][e^-] = k_{DR}([HO_2^+] + [H_3^+] + [H_2^+])$. Substituting this expression into the steady-state expression for $[H_2^+]$ and ignoring the dissociative recombination of H_2^+ ($k_7[e^-] << k_2[O_2] + k_3[H_2]$) results in the following:

$$[H_2^+] = \frac{k_{DR}([H_3^+] + [HO_2^+])[e^-]}{k_2[O_2] + k_3[H_2]}$$

Using this expression, the ratio of H_2^+ over the sum of H_3^+ and HO_2^+ is found to be equal to $\frac{k_{DR}[e^-]}{k_2[O_2]+k_3[H_2]}$. This expression can be numerically solved by using the electron density from the work of Cordonnier *et al.* [8] and the calculated number densities for H_2 and O_2 and rate constants from Table 4.1. Given these values, the ratio of H_2^+ to the other positive ions formed in the plasma is estimated to be on the order 10^{-4} and thus, H_2^+ is a minor ion at steady-state.

From this, it can be concluded that H_2^+ can be neglected in the two remaining steady-state expressions for H_3^+ and HO_2^+. Additionally, the electron recombination terms of HO_2^+ and H_3^+ are small when compared to the other terms in the denominator, and therefore, they can be neglected as well. These assumptions result in the following expressions for H_3^+ and HO_2^+:

$$[H_3^+] = \frac{k_{-4}[HO_2^+][H_2]}{k_4[O_2]}$$

$$[HO_2^+] = \frac{k_4[H_3^+][O_2]}{k_{-4}[H_2]}$$

Using either of these expressions, an expression for the estimated steady-state number density of HO_2^+ can be derived and is as follows:

$$[HO_2^+] = \frac{k_4}{k_{-4}}\frac{[O_2]}{[H_2]}[H_3^+]$$

This final expression demonstrates that reaction 4.1 is dominant over all other reactions. In addition, this simplified expression can be used to estimate the number density of HO_2^+. First, the term $\frac{k_4}{k_{-4}}$ is defined

to be the equilibrium constant, K. From the previous study by Widicus Weaver *et al.* [66], the equilibrium constant as a function of temperature can be obtained. The total ion density generated in a hydrogenic positive column discharge can be obtained from the works of Cordonnier *et al* [8] and the estimated H_3^+ ion density for hydrogen-oxygen plasma can be calculated. Finally, the number density of O_2 is assumed to be equivalent to the number density of H_2 for an initial 1:1 ratio of oxygen:hydrogen (Table 4.1). Using these values, the HO_2^+ number density is approximately 2.0×10^{10} cm^{-3}. It is important to note that since the HO_2^+ number density is proportional to O_2 number density, an increase in the amount of oxygen will result in an increase in the HO_2^+ density. Similarly, the HO_2^+ number density is inversely proportional to the H_2 number density and therefore, decreasing the amount of hydrogen will also result in an increase in the HO_2^+ number density. However, it should be also noted that decreasing the hydrogen content too much will cause the previous assumption that the H_2^+ terms are small and therefore neglected to be invalid.

The next step in the signal-to-noise ratio calculation is to determine an individual line strength that would be expected from the HO_2^+ ion. A simulation of the target band, ν_2, was performed in PGopher (see Figure 4.4) [64]. An asymmetric top with C_s ground state geometry was assumed and rotational constants were taken from previously published values [66]. Figure 4.4 is the resulting simulation for a plasma at 450 K. By the use of one of the strongest transitions ($6_{16} \leftarrow 7_{07}$), a ratio can be calculated by dividing the intensity of the transition by the total band intensity. This calculated ratio can then be multiplied by the reported total band strength of 544 km/mol to calculate the individual line strength [46]. Using this method, the line strength of this transition is calculated to be 8.47×10^{-20} cm/molecule.

By combining the estimated number of density of HO_2^+ and the expected line strength, it is possible to calculate the expected signal-to-noise ratio that would be obtained using cavity ring-down spectroscopy. The absorption depth can be calculated as follows:

$$\text{absorptiondepth} = \frac{n \times L \times \text{linestrength}}{\text{linewidth}}$$

The value n is the calculated number density and L is the length of laser beam traversed across the plasma. The value of L is 100 cm for the positive column available in our lab. The linewidth is assumed to be equivalent to the Doppler linewidth and estimated to be 0.007 cm^{-1} at 450 K. Next, the noise is approximated by the noise equivalent absorption depth from the following equation:

$$\text{NEADepth} = \sigma \times \text{cavitylength}$$

For cavity ringdown spectroscopy, σ is approximately 1×10^{-8} cm^{-1} and the cavity length is the length of

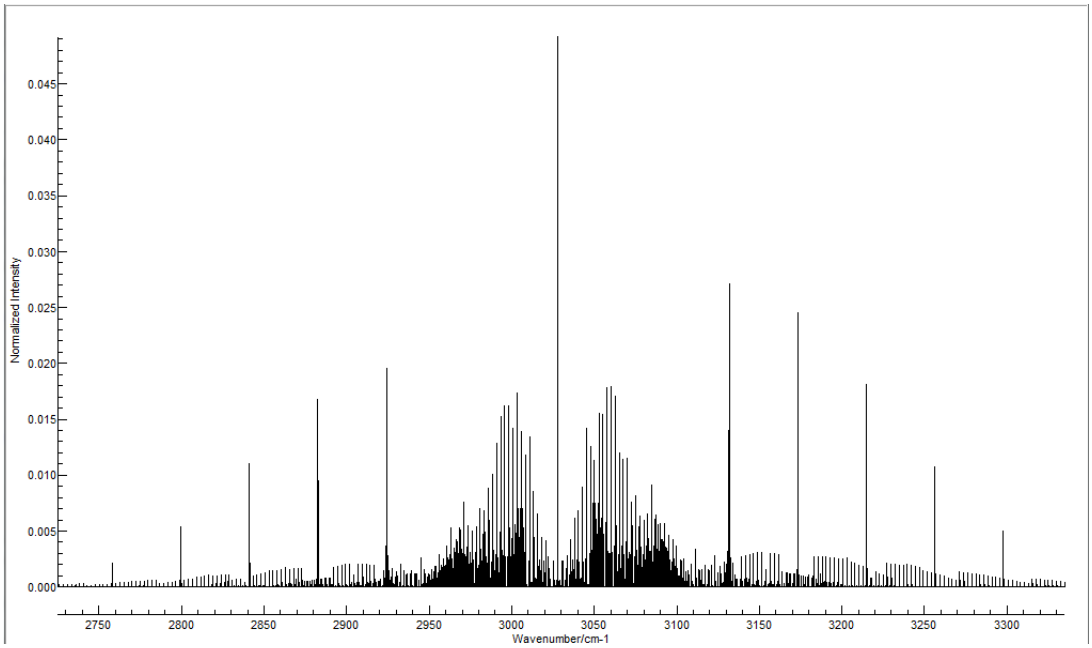

Figure 4.4: Simulation of the ν_2 fundamental band of HO_2^+ at 450 K.

the positive column or L. Dividing the absorption depth by the noise equivalent absorption depth yields an expected signal-to-noise ratio. Given the above conditions, the signal-to-noise ratio is approximately 24. With this calculated value, the detection of numerous lines (¿100) arising from the ν_2 fundamental band of HO_2^+ is ensured.

It is important to note the potential sources of errors in this calculation. First, some side reactions are ignored, but are expected to change the number density of the generated HO_2^+ ion much less than an order of magnitude. Next, the temperature is assumed to be 450 K. If a lower temperature could be achieved, this would result in a decrease in the rate of reaction 4.1 and thus, the number density of HO_2^+. However, the line strength is expected to increase with a decrease in temperature. The net effect of these two changes will result in a slight increase in the estimated signal-to-noise ratio (30 for 200 K plasma). On this note, it would be important to consider the use of a hollow cathode cell. Not only do these cells effectively cool the plasma to much lower temperatures, but they also generate a much higher ion density. The combination of these two conditions would increase the signal-to-noise ratio ($\approx$ 600 for 200 K plasma with a total ion density of 5.9×10^{11} cm^{-3} [**?**]). There is one caveat in the use of a hollow cathode cell; the copper tubing inside our current hollow cathode cell will be oxidized in an oxygen plasma. The extent of this oxidation is unknown, but can be reversed by flowing hydrogen gas through the cell. In order to determine the viability of the hollow cathode with this investigation, it would be necessary to test generating an oxygen plasma or modify the current cathode to a material that does not oxidize as readily. Finally, all numbers are an estimation

of experimentally determined values. Upon set-up of the experimental apparatus, these values can be more accurately determined.

4.3 Proposed Investigation

The final objective of this chapter is to outline a proposed experimental investigation. The plasma will be generated in a liquid-nitrogen cooled positive column that is available in our lab. The use of a hollow cathode cell should also be considered. The feed gas will initially be comprised of an oxygen:hydrogen ratio of 1:1 that is diluted in helium. Total cell pressure should range from 1-10 Torr depending on the stability of plasma. The oxygen:hydrogen ratio should be adjusted to produce more of the desired ion. As shown previously, increasing the oxygen content should increase the production of HO_2^+.

To probe the species generated in the plasma, a mid-infrared laser beam is needed. Given the availability of a mid-infrared laser system that is described in Chapter 2, the ν_2 fundamental band will be probed. Due to the uncertainty in the band center as discussed in the previous sections, broad scans (100-200 cm^{-1}) centered around the most recent calculated frequency of 3028 cm^{-1} will be performed. The spectroscopic technique to be employed will be cavity ringdown spectroscopy. However, a recent technique may be considered for this investigation: cavity-enhanced velocity modulation spectroscopy (CEVMS) [57]. This technique combines the ability to discriminate between ions and neutrals in addition to increasing the sensitivity of the spectroscopy with the addition of the cavity. Details of this spectroscopic technique can be found in a recent publication [57].

In summation, a proposed experimental investigation of HO_2^+ ion is outlined. The detection of this species will provide spectroscopists with a spectrum of the elusive HO_2^+, and serve as an initial starting point in understanding the chemistry of this species. With further advancement in receiver technology, astronomers can also use this experimental spectrum to guide observational studies of this ion and gain a better understanding of the interstellar concentration of O_2. Despite the fact that this ion has eluded detection for over three decades, the combination of the described sensitive spectroscopic technique as well as a prediction of the plasma chemistry should yield the first experimental spectrum of the HO_2^+ ion.

Bibliography

[1] T. Amano. *J. Opt. Soc. Am. B*, **2**(5):790, 1985.

[2] T. Amano. *J. Chem. Phys.*, **92**(11):6492, 1990.

[3] R. Berman, A. H. Cooke, and R .W. Hill. *Annu. Rev. Phys. Chem.*, **7**(1):1, 1956.

[4] M. Bonitz, N. Horing, and P. Ludwig. *Introduction to Complex Plasmas*. Springer, 2010.

[5] T. Bridigum. *How To Weld*. Motorbooks Workshop. Motorbooks, 2008.

[6] S. I. B. Cartledge, G. C. Clayton, K. D. Gordon, B. L. Rachford, B. T. Draine, P. G. Martin, J. S. Mathis, K. A. Misselt, U. J. Sofia, D. C. B. Whittet, and M. J. Wolff. *Astrophys. J.*, **630**(1):355, 2005.

[7] J. Chen, S. Park, Z. Fan, J.G. Eden, and C. Liu. *Microelectromechanical Systems*, **11**(5):536, 2002.

[8] M. Cordonnier, D. Uy, R. M. Dickson, K. E. Kerr, Y. Zhang, and T. Oka. *J. Chem. Phys.*, **113**(8):3181, 2000.

[9] K. N. Crabtree, N. Indriolo, H. Kreckel, B. A. Tom, and B. J. McCall. *Astrophys. J.*, **729**(1):15, 2011.

[10] K. N. Crabtree, C. A. Kauffman, B. A. Tom, E. Beçka, B. A. McGuire, and B. J. McCall. *J. Chem. Phys.*, in press.

[11] K. N. Crabtree, B. A. Tom, and B. J. McCall. *J. Chem. Phys.*, in press.

[12] A. Dalgarno, J.H. Black, and J.C. Weisheit. *Astrophysical Letters*, **14**:77, 1973.

[13] D. J. DeFrees and A. D. McLean. *J. Chem. Phys.*, **82**(1):333, 1985.

[14] A. Dinklage. *Plasma physics: confinement, transport and collective effects*. Lecture notes in physics. Springer, 2005.

[15] P. Drossart, J.-P. Maillard, J. Caldwell, S. J. Kim, J. K. G. Watson, W. A. Majewski, J. Tennyson, S. Miller, S. K. Atreya, J. T. Clarke, J. H. Waite, and R. Wagener. *Nature*, **340**(6234):539, 1989.

[16] J. M. Dyke, N. B. H. Jonathan, A. Morris, and M. J. Winter. *Mol. Phys.*, **44**(5):1059, 1981.

[17] Cornelia Fischer and Markus Sigrist. Mid-IR difference frequency generation. In Irina Sorokina and Konstantin Vodopyanov, editors, *Solid-State Mid-Infrared Laser Sources*, volume 89 of *Topics in Applied Physics*, pages 99–143. Springer Berlin / Heidelberg, 2003.

[18] A. Fried and D. Richter. *Infrared Absorption Spectroscopy*. Blackwell Publishing, 2007.

[19] C. M. Gabrys, D. Uy, M.-F. Jagod, T. Oka, and T Amano. *J. Phys. Chem.*, **99**(42):15611, 1995.

[20] T. R. Geballe and T. Oka. *Nature*, **384**(6607):334, 1996.

[21] T.R. Geballe, M.-F. Jagod, and T. Oka. *Astrophys. J.*, **408**(2 PART 2):L109, 1993.

[22] T.R. Geballe, B.J. Mccall, K.H. Hinkle, and T. Oka. *Astrophys. J.*, **510**(1 PART 1):251, 1999.

[23] D. Gerlich. *J. Chem. Phys.*, **92**(4):2377, 1990.

[24] D. Gerlich. *J. Chem. Soc., Faraday Trans.*, **89**(13):2199, 1993.

[25] D. Gerlich, E. Herbst, and E. Roueff. *Planet. Space Sci.*, **50**(12-13):1275, 2002.

[26] E. Herbst and Klemperer .W. Formation. *Astrophys. J.*, **185**(2):505, 1973.

[27] W. C. Ho, C. J. Pursell, and T. Oka. *Mol. Spectrosc.*, **149**(2):530, 1991.

[28] T. R. Hogness and E. G. Lunn. *Phys. Rev.*, **26**(1):44, 1925.

[29] E. Hugo, O. Asvany, and S. Schlemmer. *J. Chem. Phys.*, **130**(16):164302, 2009.

[30] N. Indriolo, T. R. Geballe, T. Oka, and B. J. McCall. *Astrophys. J.*, **671**(2):1736, 2007.

[31] R. Johnsen, C. Huang, and M. A. Biondi. *J. Chem. Phys.*, **65**(4):1539, 1976.

[32] J. H. Lacy, R. Knacke, T. R. Geballe, and T. Tokunaga. *Astrophys. J.*, **428**:L69, 1994.

[33] J. H. Van Lenthe and P. J. A. Ruttink. *Chem.Phys. Lett.*, **56**(1):20, 1978.

[34] C.M. Lindsay and B. J. McCall. *Mole. Spectrosc.*, **210**(1):60, 2001.

[35] B. J. McCall. *Spectroscopy of H_3^+ in Laboratory and Astrophysical Plasmas.* PhD thesis, University of Chicago, 2001.

[36] B. J. McCall, T. R. Geballe, K. H. Hinkle, and T. Oka. *Science*, **279**(5358):1910, 1998.

[37] B. A. McGuire. Design and Implementation of a Liquid Nitrogen-Cooled Hollow Cathode Discharge Source for the Study of the Reaction $H_3^+ + H_2 \rightarrow H_2 + H_3^+$ at Physically Relevant Temperatures. B. S. Thesis, University of Illinois at Urbana-Champaign, 2009.

[38] S. Miller, T. Stallard, H. Melin, and J. Tennyson. *Faraday Disc.*, **147**:283, 2010.

[39] S. A. Nizkorodov, D. Roth, R. V. Olkhov, J. P. Maier, and O. Dopfer. *Chem. Phys. Lett.*, **278**(1-3):26, 1997.

[40] T. Oka. *Mole. Spectrosc.*, **228**(2):635, 2004.

[41] T. Oka. *Proc. Natl. Acad. Sci. U.S.A.*, **103**(33):12235, 2006.

[42] K. Park and J. C. Light. *J. Chem. Phys.*, **126**(4):044305, 2007.

[43] F. Paschen. *Ann. Phys.*, **355**(16):901, 1916.

[44] W. Paul, B. Lücke, S. Schlemmer, and D. Gerlich. *In. J. Mass Spec. and Ion Proc.*, **149-150**(C):373, 1995.

[45] M. Quack. *Mole. Phys.*, **34**(2):477, 1977.

[46] G. E. Quelch, Y. Xie, B. F. Yates, Y. Yamaguchi, and H. F. Schaefer. *Mole. Phys.*, **68**(5):1095, 1989.

[47] G. Meijer R. Peeters, G. Berden. *Am. Lab.*, **33**:60, 2001.

[48] B. L. Rachford, J. M. Shull W. P. Blair R. Ferlet S. D. Friedman C. Gry E. B. Jenkins D. C. Morton B. D. Savage P. Sonnentrucker A. Vidal-Madjar D. E. Welty T. P. Snow, J. Tumlinson, and D. G. York. *Astrophys. J.*, **577**(1):221, 2002.

[49] B. L. Rachford, T. L. Ross R. Ferlet S. D. Friedman C. Gry E. B. Jenkins D. C. Morton B. D. Savage J. M. Shull P. Sonnentrucker J. Tumlinson A. Vidal-Madjar D. E. Welty T. P. Snow, J. D. Destree, and D. G. York. *Astrophys. J. Suppl.*, **180**(1):125, 2009.

[50] J. C. Raich and R. H. Good. *Astrophys. J.*, **139**:1004, 1964.

[51] G. P. Raine, H. F. Schaefer III, and N. C. Handy. *J. Chem.Phys.*, **80**(1):319, 1984.

[52] J. M. Robbe, M. Monnerville, G. Chambaud, P. Rosmus, and P. J. Knowles. *Chem. Phys.*, **252**(1-2):9, 2000.

[53] M. Saporoschenko. *Phys. Rev.*, **139**(2A):A349, 1965.

[54] B. D. Savage, R. C. Bohln, J.F. Drake, and W. Budich. *Astrophys. J.l*, **216**:291–307, 1977.

[55] Y. Sheffer, M. Rogers, S. R. Federman, N. P. Abel, R. Gredel, D. L. Lambert, and G. Shaw. *Astrophys. J.*, **687**(2):1075, 2008.

[56] J. M. Shull, J. Tumlinson, E. B. Jenkins, H. W. Moos, B. L. Rachford, B. D. Savage, K. R. Sembach, T. P. Snow, G. Sonneborn, D. G. York, W. P. Blair, J. C. Green, S. D. Friedman, and D. J. Sahnow. *Astrophys. J. Lett.*, **538**(1):L73, 2000.

[57] B.M. Siller, A.A. Mills, and B.J. McCall. *Opt. Lett.*, **35**(8):1266, 2010.

[58] R. Spangenburg and D.K. Moser. *Niels Bohr: Atomic Theorist*. Chelsea House, 2008.

[59] J. J. Thomson. *Phil. Mag.*, **21**:225, 1911.

[60] B. A. Tom. *Nuclear Spin Dependence in Reactions of H_3^+ in the Laboratory and the Interstellar Medium*. PhD thesis, University of Illinois at Urbana-Champaign, 2009.

[61] B. A. Tom, S. Bhasker, Y. Miyamoto, T. Momose, and B. J. McCall. *Rev. Sci. Instrum.*, **80**(1):016108, 2009.

[62] L.M. Trafton, T.R. Geballe, S. Miller, J. Tennyson, and G.E. Ballester. *Astrophysical Journal*, **405**(2):761, 1993.

[63] W. D. Watson. *Astrophys. J.*, **83**(1):L17, 1973.

[64] C. M. Western. Pgopher, a program for simulating rotational structure. Version 7.1, 2010.

[65] J. U. White. *J. Opt. Soc. Am.*, **32**(5):285, 1942.

[66] S. L. Widicus Weaver, D. E. Woon, B. Ruscic, and B. J. McCall. *Astrophys. J.*, **697**(1):601, 2009.

[67] E. Wigner. *Z. f. Phys. Chem.*, **23**:28, 1933.

[68] J. Woddall, M. Agundez, A. J. Markwick-Kemper, and T. J. Millar. The UMIST Database for Astrochemistry.